Geochemistry Geophysics Geosystems G3
AN ELECTRONIC JOURNAL OF THE EARTH SCIENCES
Published by AGU and the Geochemical Society

Article
Volume 10, Number 5
15 May 2009
Q05W02, doi:10.1029/2008GC002345
ISSN: 1525-2027

Adjoint models of mantle convection with seismic, plate motion, and stratigraphic constraints: North America since the Late Cretaceous

Sonja Spasojevic, Lijun Liu, and Michael Gurnis
Seismological Laboratory, California Institute of Technology, Pasadena, California 91125, USA (sonja@gps.caltech.edu)

[1] We apply adjoint models of mantle convection to North America since the Late Cretaceous. The present-day mantle structure is constrained by seismic tomography and the time-dependent evolution by plate motions and stratigraphic data (paleoshorelines, borehole tectonic subsidence, and sediment isopachs). We infer values of average upper and lower mantle viscosities, provide a synthesis of North American vertical motions (relative sea level) from the Late Cretaceous to the present, and reconstruct the geometry of the Farallon slab back to the Late Cretaceous. In order to fit Late Cretaceous marine inundation and borehole subsidence, the adjoint model requires a viscosity ratio across 660 km discontinuity of 15:1 (reference viscosity of 10^{21} Pa s), which is consistent with values previously inferred by postglacial rebound studies. The dynamic topography associated with subduction of the Farallon slab is localized in western North America over Late Cretaceous, representing the primary factor controlling the widespread flooding. The east coast of the United States is not stable; rather, it has been experiencing continuous dynamic subsidence over the Cenozoic, coincident with an overall eustatic fall, explaining a discrepancy between sea level derived from the New Jersey coastal plain and global curves. The east coast subsidence further constrains the mantle viscosity structure and requires an uppermost mantle viscosity of 10^{20} Pa s. Imposed constraints require that the Farallon slab was flat lying during Late Cretaceous, with an extensive zone of shallow dipping Farallon subduction extending beyond the flat-lying slab farther east and north by up to 1000 km than previously suggested.

Components: 13,315 words, 13 figures, 2 tables.

Keywords: adjoint mantle convection models; dynamic topography; continental subsidence; Western Interior Seaway.

Index Terms: 8120 Tectonophysics: Dynamics of lithosphere and mantle: general (1213); 9350 Geographic Location: North America; 8162 Tectonophysics: Rheology: mantle (8033).

Received 1 December 2008; **Revised** 30 March 2009; **Accepted** 3 April 2009; **Published** 15 May 2009.

Spasojevic, S., L. Liu, and M. Gurnis (2009), Adjoint models of mantle convection with seismic, plate motion, and stratigraphic constraints: North America since the Late Cretaceous, *Geochem. Geophys. Geosyst.*, *10*, Q05W02, doi:10.1029/2008GC002345.

Theme: Plate Reconstructions, Mantle Convection, and Tomography Models: A Complementary Vision of Earth's Interior
Guest Editors: D. Muller, S Quere, and T. Torsvik

1. Introduction

[2] The Cretaceous marine inundation of western North America (NAM) has been a stratigraphic enigma because of the combination of large thicknesses of sediments deposited over a large horizontal length scale (nearly 10^3 km) [*Bond*, 1976; *Cross and Pilger*, 1978; *Liu and Nummedal*, 2004; *Liu et al.*, 2005]. Using hypsometric analysis and assuming isostasy, *Bond* [1976] suggests that the observed flooding of NAM (45% by area), would have required a 310 m sea level rise, resulting in the accumulation of approximately 700 m of sediments. Since nearly half of the area of NAM Cretaceous marine sediments is significantly thicker than 700 m, *Bond* [1976] argued that eustasy could not have been the only process that had operated. *Cross and Pilger* [1978] attributed the excessive sediment thickness and subsidence to subcrustal loading induced by a shallow dipping slab. *Liu et al.* [2005] determine that regional subsidence of the Western Interior consists of a short-wavelength flexural loading component that changed on a time scale of a few million years, and a long-wavelength dynamic component that changed over a time scale of tens of million years. *Liu and Nummedal* [2004] determine that the wavelength of the dynamic subsidence component is on the order of 1500 km.

[3] Cretaceous marine sediments at present lie at an elevation of approximately 1 km, but since putative long-term global sea levels vary from 70 m [*Miller et al.*, 2005] to 250 m [*Haq and Al-Qahtani*, 2005], NAM must have subsided and then uplifted over a large length scale [*Bond*, 1976]. Several numerical models have attempted to explain these inferred vertical motions in terms of the dynamic topography induced by negatively buoyant subducted slabs [*Mitrovica et al.*, 1989; *Burgess et al.*, 1997; *Lithgow-Bertelloni and Gurnis*, 1997]. *Mitrovica et al.* [1989] attributed the Western Interior Seaway (WIS) to shallow subduction of the Farallon plate that could create a ~1,400 km wide region of dynamic subsidence. Specifically, using 2-D isoviscous forward models, subsidence and subsequent uplift was attributed to changes in the dip angle of the Farallon plate. *Burgess et al.* [1997] expanded on this concept with three-dimensional, variable viscosity models that attempted to match stratigraphic sequence boundaries. These models shared the common attributes of fixing the dynamics to the frame of reference of the overriding (NAM) plate, and fits to the stratigraphic constraints were obtained by changing the subduction depth and dip to obtain the best fits to either continental tilt [*Mitrovica et al.*, 1989] or sediment thickness and sequence boundaries [*Burgess et al.*, 1997]. *Lithgow-Bertelloni and Gurnis* [1997] used a parameterized global mantle flow model with the slabs falling vertically at a constant rate, in which NAM subsided and then uplifted as it moved to the west over the Farallon slab. However, the subsidence and uplift were phase shifted by about 20 Ma in the models toward the present compared to the inferred timings [*Lithgow-Bertelloni and Gurnis*, 1997]. *Le Stunff and Ricard* [1997] proposed that partial advection of mantle equidensity surfaces by vertical motion induced by driving loads enables better prediction of the amplitude and phase of flooding.

[4] The Farallon slab may have also influenced the stratigraphic record further to the east and later in time. By deconvolving the influence of paleobathymetry from sediment accumulation within five wells from the New Jersey coastal plain, *Miller et al.* [2005] estimated a maximum long-term sea level change of 70 m between the Late Cretaceous and the present, an amplitude that is significantly smaller than other published global estimates [e.g., *Kominz*, 1984; *Haq et al.*, 1987; *Müller et al.*, 2008b]. With higher-resolution seismic tomography [*Grand et al.*, 1997; *Van der Hilst et al.*, 1997; *Ren et al.*, 2007], the Farallon slab is resolved in the present-day at midmantle depths as a high seismic velocity anomaly beneath eastern NAM. In this paper, we investigate if both extensive Cretaceous flooding of the interior of NAM and the discrepancy between the *Miller et al.* [2005] sea level estimates and other putatively eustatic estimates can be explained by a single geodynamic model that includes the dynamic effect of Farallon slab subduction. This paper is a detailed investigation of this problem; preliminary results for the inversion of the flat slab phase of Farallon subduction [*Liu et al.*, 2008] and the subsidence of the U.S. east coast [*Spasojević et al.*, 2008] have recently appeared.

[5] We combine advances in mantle convection modeling with stratigraphy, plate motion and seismic tomography to better understand the relation of Farallon plate subduction and vertical motions and long-term sea level change. We use the concept of separate frames of reference for the mantle and plate to better link vertical motions to the stratigraphic record, as demonstrated for the evolution of Australia [*Gurnis et al.*, 1998]. Second, in order to use the seismic constraints

directly we implement adjoint (inverse) models of convection [*Bunge et al.*, 2003; *Ismail-Zadeh et al.*, 2004; *Liu and Gurnis*, 2008]. Third, we use a new generation of plate reconstructions in which plate margins continuously change with plate motion (M. Gurnis et al., Global plate reconstructions with continuously closing plate, manuscript in preparation, 2009). The dynamic models are constrained by observations of paleoshorelines [*Smith et al.*, 1994; *Bond*, 1978], borehole tectonic subsidence [*Pang and Nummedal*, 1995; *Liu and Nummedal*, 2004; *Liu et al.*, 2005] and isopach thickness [*Cook and Bally*, 1975] in the WIS. In addition, we test the models through the Cenozoic vertical motions of the eastern United States using paleoshoreline analyses [*Spasojević et al.*, 2008] and borehole-inferred, regional sea level variations [*Van Sickel et al.*, 2004; *Miller et al.*, 2005].

[6] Our new results include empirical analysis of correlation between stratigraphy and seismic tomography, inferred values of effective temperatures of the Farallon slab, a preferred viscosity profile using stratigraphic constraints, and a post Late Cretaceous differentiation between (dynamic) relative sea level and eustatic factors for NAM. In addition, we compare our model predictions against inferred sediment thicknesses for the western Canadian shield from the thermochronology of basement samples [*Flowers*, 2009].

2. Observational Constraints

2.1. Tomography

[7] Seismic tomography constrains present-day mantle convection, including the Farallon slab. Global seismic tomography inversions reveal linear positive seismic anomalies beneath the Americas with shear (S) [*Grand et al.*, 1997] and compressional (P) waves [*Van der Hilst et al.*, 1997]. Although more blurred, global models with spherical harmonic basis functions also detect this structure [*Megnin and Romanowicz*, 2000; *Ritsema et al.*, 2004]. Recent regional models that invert both S and P wave travel times [*Ren et al.*, 2007] or use multiple-frequency P wave tomography [*Sigloch et al.*, 2008] reveal the Farallon remnants with similar geometries. Given uncertainties in the detailed structure of the slab and differences between S and P sensitivity, all these models, especially ones with block basis functions, agree on the spatial distribution, wavelength, and magnitude of the anomaly. The present-day Farallon remnant largely strikes north-south along the North American east coast from Central America to the Arctic. In a map view, it has a width of 500–1,000 km while extending from 800 to 2,000 km depth with typical S wave anomaly of about 1%. In this study, we use an updated version of a shear wave model [*Grand*, 2002].

[8] To convert tomography into density, we first remove the signal above 250 km that correlates with the craton, assuming it is neutrally buoyant [*Jordan*, 1975; *Goes and van der Lee*, 2002]. Because we consider differential dynamic topography, removal of this layer will not affect our results. If this structure were attached to the moving plate and neither local convective instability nor thickening/thinning of the layer were significant, it would not change topography. We also remove seismic structures below 2,400 km depth, where there is a clear gap in the seismic image. From 2,400 km up to 800 km, we adopt a constant density to velocity perturbation ratio (section 4.1 and equation (5)), constrained by vertical motions.

2.2. Continental Stratigraphy and Sea Level

[9] The WIS has relatively well preserved Cretaceous sediments, mapped in outcrops and boreholes. As constraints to dynamic models, we use paleoshorelines [*Smith et al.*, 1994; *Bond*, 1978], borehole tectonic subsidence curves [*Pang and Nummedal*, 1995; *Liu et al.*, 2005] and a Late Cretaceous isopach [*Cook and Bally*, 1975]. The WIS started developing in early Cretaceous by southward transgression from the Arctic and northward transgression from the Gulf of Mexico [*Sloss*, 1988]. By Late Cretaceous the WIS (Figure 1) developed into a large epicontinental sea stretching from the Gulf of Mexico to the Arctic, and having a width of thousands of kilometers east-west [*Smith et al.*, 1994]. Using the boundary between preserved marine and nonmarine sediments, *Smith et al.* [1994] defined eight paleoshorelines from Late Cretaceous to present (at 95, 85, 70, 60, 45, 30, 20, 12 Ma). During Late Cretaceous, the western edge of the seaway was located close to the Sevier belt [*Sloss*, 1988; *Liu et al.*, 2005], while the eastern shoreline migrated slightly eastward from 95 Ma (Figure 1) to 70 Ma [*Smith et al.*, 1994]. The retreat of the seaway commenced at the end of Late Cretaceous, and the inland sea withdrew completely by early Cenozoic [*Smith et al.*, 1994]. We use digitized maps of *Smith et al.* [1994] for Late Cretaceous to qualitatively constrain the position of the dynamic topography low associated with subduction, as illustrated by the 95 Ma shoreline reconstruction (Figure 1). We also use recon-

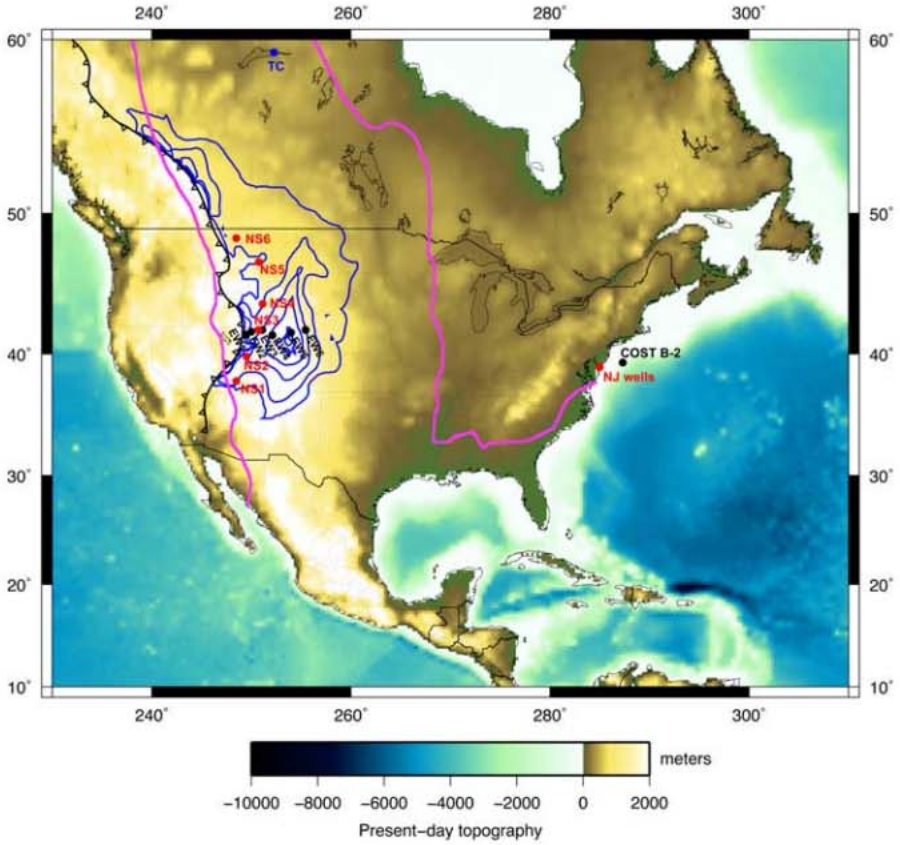

Figure 1. Position of data constraints used in the study. Pink line shows reconstructed 95 Ma paleoshoreline [*Smith et al.*, 1994], blue contours show total Late Cretaceous isopach [*Cook and Bally*, 1975] with 2000 ft contour interval, and black line shows position of the Sevier thrust belt [*Cook and Bally*, 1975]. Black and red dots, marked as EW1–EW6 and NS1–NS6, indicate location of boreholes of tectonic subsidence curves [*Liu et al.*, 2005; *Pang and Nummedal*, 1995]. Red dot marked NJ wells shows position of wells located on the New Jersey coastal plain [*Miller et al.*, 2005], and black dot marked COST-B2 indicate position of the offshore well used by *Watts and Steckler* [1979] for sea level curve derivation. Blue dot marked TC indicates location of East Lake Athabasca thermochrology study of *Flowers* [2009].

structed Miocene and Eocene shorelines elevations [*Bond*, 1978; *Spasojevic et al.*, 2008] to infer dynamic subsidence of the U.S. east coast [*Spasojevic et al.*, 2008]. The total and tectonic subsidence in boreholes have been inferred from 1-D subsidence analysis after accounting for decompaction, changes in water depth, eustasy, and Airy isostatic backstripping [*Liu et al.*, 2005; *Liu and Nummedal*, 2004; *Pang and Nummedal*, 1995]. We selected a total of 12 tectonic subsidence curves, six on an east-west profile (Figure 1, locations EW1–EW6) in Wyoming [*Liu et al.*, 2005], and six representative locations from *Pang and Nummedal* [1995] (Figure 1; locations NS1 to NS6).

[10] *Cook and Bally* [1975] used outcrops and boreholes between mid Cenomanian and the top of the Maeastrichtian to define three separate isopach maps (mid Cenomanian to top Turonian; Coniacian-Santonian; Campanian-Maestrichtian). Since the spatial extent of these isopachs is similar, we use a total Late Cretaceous isopach [*Cook and Bally*, 1975] from mid Cenomanian to Maestrichtian. The area of late Cretaceous sedimentation is approximately 1,300 km wide east-west, and 3,000 km north-south (Figure 1). The maximum thickness of the total Late Cretaceous sediments is around 3 km, with the thickest sediments (Figure 1) located close to the Sevier belt [*Sloss*, 1988; *Cross and Pilger*, 1978]. The oldest isopach (Upper Albian to Santonian strata) is thickest along a north-south trending depositional trough parallel to the Sevier belt [*Cross and Pilger*, 1978]. The remaining Upper Albian to Santonian strata occurs more broadly with thicknesses diminishing to the east [*Cross and Pilger*, 1978]. The younger isopach (Santonian to Maestrichtian) was deposited throughout most of the WIS, with its center in a broad region of southern Wyoming, northwestern and north central Colorado

and eastern Utah [*Cross and Pilger*, 1978]. There was no prominent linear depositional trough parallel to the Sevier belt in the Santonian to Maestrichtian [*Cross and Pilger*, 1978].

[11] There is significant disagreement on the amplitude of eustasy since the Late Cretaceous with maximum long-term estimates varying between 70 m [*Miller et al.*, 2005] to more than 250 m [*Haq et al.*, 1987]. *Miller et al.* [2005] made sea level estimates based on the backstripping of sedimentary sections at five boreholes on the New Jersey coastal plain [*Van Sickel et al.*, 2004] with the maximum long-term sea level around 70 m. High estimates of sea level with a maximum on order of 250–300 m are based on global correlations of stratigraphic sequences [*Haq et al.*, 1987; *Haq and Al-Qahtani*, 2005]. Low estimates of 120 m are based on backstripping of wells on the eastern NAM continental margin [*Watts and Steckler*, 1979]. *Kominz* [1984] estimates global sea level from changing mid ocean ridge volume, which matches sea level required to flood continental interiors, especially since the Eocene [*Bond*, 1979; *Harrison*, 1990]. The maximum amplitude of sea level change according to *Kominz* [1984] is 220 m, slightly higher than 213 m from an updated estimate [*Müller et al.*, 2008b].

2.3. Plate Motions

[12] We use GPlates reconstructions of global plate motions at 1 Ma intervals, in which the plate margins continuously evolve with self-consistent velocities between plates and plate margins (Gurnis et al., manuscript in preparation, 2009). The rotation poles of *Müller et al.* [2008a] are used, implemented in a moving hot spot reference frame.

[13] There has been significant discussion of the influence of absolute reference frames on convection models [e.g., *Quère and Forte*, 2006]. The hot spot reference frame [*Morgan*, 1971] is originally based on the hypothesis that hot spots originate from plumes that are fixed relative to the mantle with no relative motion between them. The moving hot spot reference frame corrects for known relative motion between different groups of hot spots [*O Neill et al.*, 2005], which results in significantly different plate motions compared to the fixed reference frames prior to 80 Ma. The no-net-rotation reference frame [*Solomon and Sleep*, 1974] assumes uniform coupling between lithosphere and asthenosphere. *Conrad and Husson* [2009] propose that the sea level estimates from dynamic models can be influenced by the implementation of different absolute reference frames. However, since we are examining dynamic effects of Farallon slab subduction on NAM regional vertical motion, we ensure that the reference frame we utilize is appropriate by requiring that temporal and spatial evolution of subsidence and uplift is well correlated by NAM observations, as we will describe below.

[14] The reconstructions are global, but some of the details within the NAM region are as follows. At 100 Ma, the western margin of NAM is continuously converging from north to south. This persists to 31 Ma, when the Farallon-Pacific ridge intersects the Farallon-NAM trench [*Atwater and Stock*, 1998], and the San Andreas Fault forms by a small jump to the east in California. The transform segment enlarges at the expense of the convergent margin [*Atwater and Stock*, 1998] and the Juan de Fuca to the north and the Cocos plates to the south continuously shrink (Figure 2). In the south of our region, the Caribbean reconstruction closely follows that of *Pindell et al.* [2006]. From 100 to 80 Ma, North and South America are separated by a spreading center, while the Caribbean region grows by the eastward motion of the Farallon plate between North and South America. At 60 Ma, a new trench and island arc initiates to subsequently become the western margin of southern Mexico and Central America [*Pindell et al.*, 2006].

3. Simple Sedimentary-Tomography Correlations

[15] If the anomalous Late Cretaceous vertical motions were indeed related to dynamic topography associated with Farallon subduction, then correlations between the stratigraphic record and Farallon slab imaged by seismic tomography may be revealing. The Farallon slab is well defined at mid mantle depths (800, 1,225 and 1,675 km) as a positive S wave velocity anomaly, while the position of the slab is less evident at a depth of 1,975 km (Figure 2). Paleoshorelines and sediment isopachs rotated to mantle frame of reference are poorly correlated with the position of the slab at 800 km and 1,975 km (Figure 2). Isopach at 100 Ma correlates well with positive seismic anomaly at 1,675 km, while the 70 Ma isopach and shoreline are moderately well correlated with positive seismic anomaly at 1,225 km. Assuming that the positive seismic anomaly corresponds to the subducted Farallon slab, we can infer that the originally shallow-dipping slab causing flooding in the WIS has been subducted to depths of approximately 1,200–1,700 km.

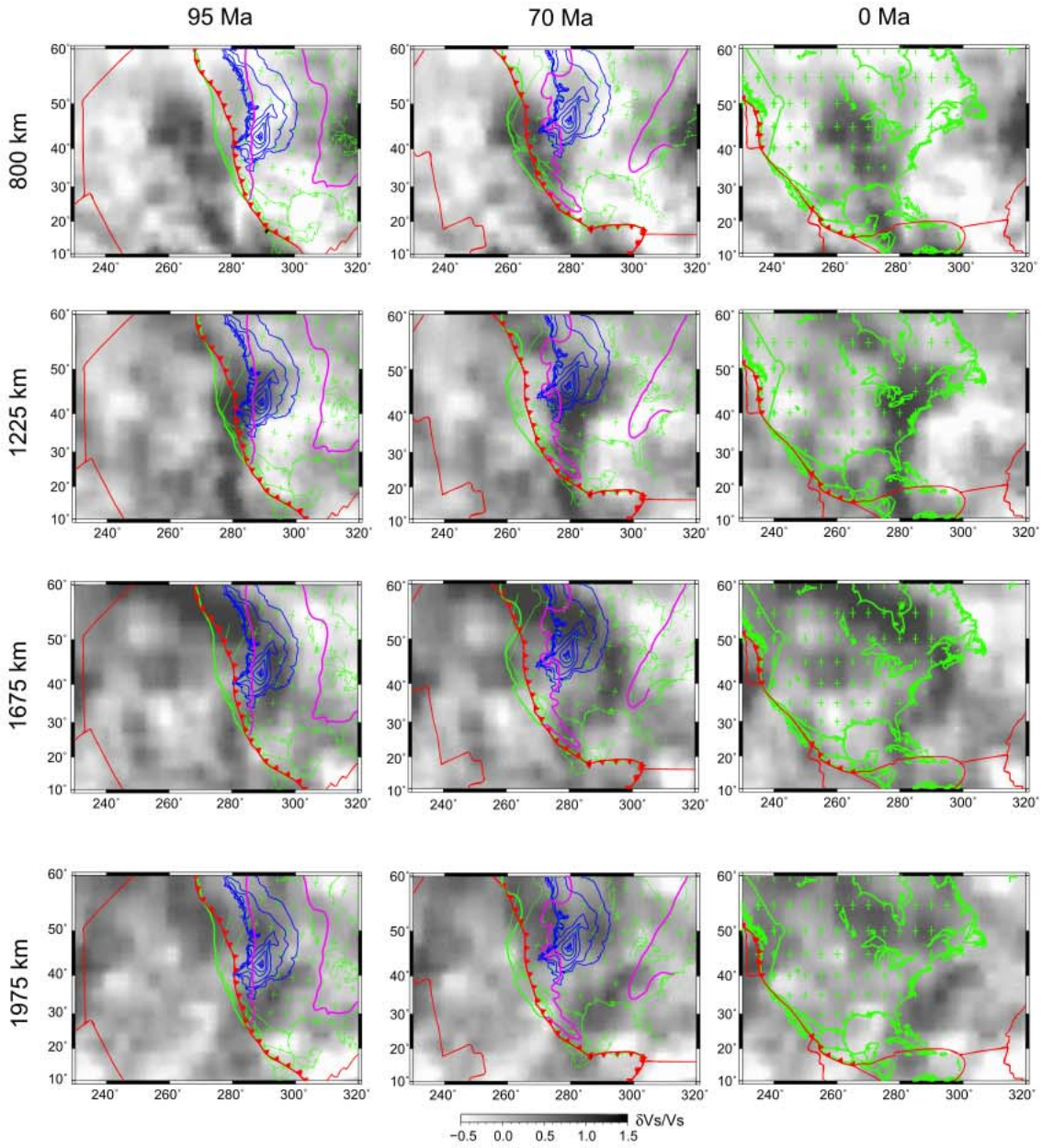

Figure 2. Map view of correlation between present-day seismic tomography [*Grand*, 2002] and total Late Cretaceous isopach [*Cook and Bally*, 1975] rotated back 95 and 70 Ma to mantle frame of reference. Positive seismic anomaly associated with the Farallon slab is shown with dark gray shading, blue lines show total Late Cretaceous isopach contours [*Cook and Bally*, 1975] with 2000 ft contour interval, and pink line indicates position of 95 Ma shoreline [*Smith et al.*, 1994]. Red lines show position of reconstructed plate boundaries from GPlates (Gurnis et al., manuscript in preparation, 2009).

[16] We define the correlation, $C(d, t)$, between total Late Cretaceous isopach and seismic tomography at age t as:

$$C(d;t) = \frac{1}{N}\sum_{n=1}^{N} S(n;t)\cdot\frac{dV_s}{V_s}(n;d) \qquad (1)$$

where $S(n, t)$ is isopach thickness and dV_s/V_s is seismic velocity anomaly at depth d, where the summation is taken over N grid points. We systematically determine $C(d, t)$ for seismic tomography at depths d = 700–2,800 km and t = 110–0 Ma. The value of isopach thickness S is always positive, while values of seismic anomaly

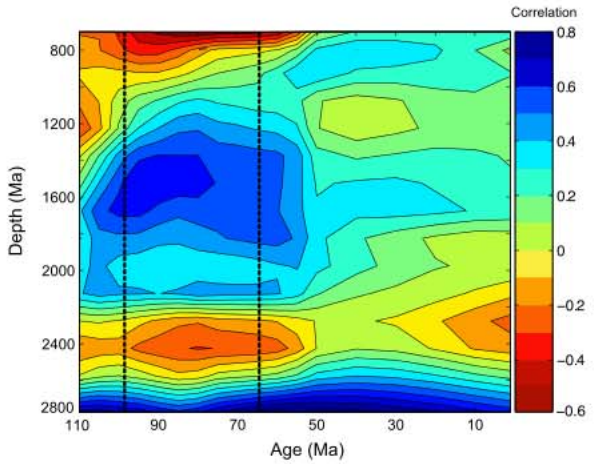

Figure 3. Correlation between seismic tomography [*Grand*, 2002] and total Late Cretaceous isopach rotated to mantle reference frame [*Cook and Bally*, 1975] for depth interval 700–2,800 km and time interval 110–0 Ma. Correlation is normalized by maximum value of $C(d, t)$.

dV_s/V_s vary between −1 and 1, with large positive values being attributed to the Farallon slab. Therefore, it is expected that maxima in $C(d, t)$ are obtained when the rotated isopach has the highest level of correlation with positive seismic anomaly associated with the Farallon slab.

[17] Isopach thickness and seismic velocity anomaly, normalized by the maximum value of C, are strongly correlated during the Late Cretaceous for depths 1,000–1,800 km (Figure 3). There is strong anticorrelation between sediment isopach and seismic tomography for the Late Cretaceous for depths shallower than approximately 1,000 km. The correlation increases with depth and reaches a maximum at around 1,500 km in the period 95–80 Ma. Maximum correlation at 100 Ma occurs at somewhat greater depths of 1,675 km. The correlation decreases for depths greater than 1,700 km, and a strong drop in the correlation at about 2,200 km depth reflects the lowest extent of the Farallon remnants in tomography. The correlation is significantly reduced for the period before 100 Ma and after 55 Ma (Figure 3).

[18] The tomography-isopach correlation is spatially and temporally well defined, with a maximum correlation at depths from 1,500 to 1,600 km, implying that this portion of the Farallon slab was probably subducting beneath the WIS during Late Cretaceous. In addition, there is a general trend of increasing depth correlating with increased age, with the 80 Ma isopach having maximum correlation at 1,525 km, and the 100 Ma isopach at 1,675 km. The increase of level of correlation close to the core-mantle boundary is due to a large area of positive seismic anomaly in this region.

4. Methodology

4.1. Adjoint Models of Mantle Convection

[19] We invert for mantle convection backward in time with a method that uses a series of forward and adjoint calculations. The forward model solves for thermal convection within an incompressible fluid with equations for conservation of mass, momentum, and energy

$$\nabla \cdot \vec{u} = 0 \tag{2}$$

$$\nabla P + \nabla \cdot (\eta \nabla \vec{u}) = \rho_m \alpha T_e \vec{g} \tag{3}$$

$$\frac{\partial T_e}{\partial t} + \vec{u} \cdot \nabla T_e = \kappa \nabla^2 T_e + H \tag{4}$$

where $\vec{u}$ is velocity, P dynamic pressure, η dynamic viscosity, ρ_m ambient mantle density, α thermal expansion coefficient, $\vec{g}$ gravitational acceleration, T_e effective temperature, κ thermal diffusivity, and H internal heat production (negligible over 100 Ma). Values of relevant parameters are given in Table 1.

[20] T_e is scaled from shear velocity anomaly through a transfer function G by

$$T_e = G(dV_s/V_s) \tag{5}$$

We refer to T_e as the effective temperature because we are unable to uniquely invert for temperature because of limited resolution of tomography and compositional controls on the shear velocity. Trade-off between seismic anomaly and grid spacing exists below the tomographic resolution, resulting in nonunique absolute seismic velocity anomalies as well as underestimates of effective temperature (assuming thermal seismic anomalies).

Table 1. Relevant Parameters Used in This Study

Parameter	Symbol	Value
Ambient mantle density	ρ_m	3340 kg/m^3
Reference viscosity	η_o	1×10^{21} Pa s
Thermal expansion coefficient	α	3×10^{-5} 1/K
Gravitational acceleration	g	9.81 m/s^2
Thermal diffusivity	κ	10^{-6} m^2/s
Earth's radius	R	6371 km
Sedimentation rate	SR	50 m/Ma

However, since dynamic topography is most sensitive to net buoyancy, the seismic ambiguity does not adversely influence our inversion. In addition to thermal effects, there is substantial chemical heterogeneity in the mantle [*Ni et al.*, 2002; *Ishii and Tromp*, 2004; *Trampert et al.*, 2004] and the mapping between seismic anomaly and temperature and density is likely to be both depth- and geography-dependent. In the adjoint models, the dynamic topography and its rate of change are sensitive to density anomalies [*Liu and Gurnis*, 2008] which could have both thermal and compositional contributions. However, since the inferred quantity is diffusive, we refer to it as "effective temperature" as opposed to "effective density". We have assumed the scaling in equation (5) is depth-independent.

[21] The mismatch between predicted temperature at the present, T_p, and the seismically inferred temperature, T_d, is

$$J = \int_V \left(T_p - T_d\right)^2 dv \qquad (6)$$

or the cost function. By solving a constrained minimization problem with its Lagrangian function constructed by appending equation (4) to equation (6) (cf. *Bunge et al.* [2003], *Ismail-Zadeh et al.* [2004], *Liu and Gurnis* [2008], and many other papers in atmospheric sciences such as *Talagrand and Courtier* [1987], *Sun et al.* [1991], and *Sirkes and Tziperman* [1997]), we get the adjoint equation

$$\frac{\partial \lambda}{\partial t} + \dot{u} \cdot \nabla \lambda + k\nabla^2 \lambda = \left(T_d - T_p\right)\delta(t - t_1) \qquad (7)$$

where λ, the Lagrangian multiplier, is the adjoint temperature and t_1 is the present time. As the conjugate operator of the forward energy equation, the adjoint model back-propagates the residual field $T_d - T_p$ to the initial time, t_0, where the corresponding velocities $\dot{u}$ are stored from the previous forward iteration [*Bunge et al.*, 2003; *Liu and Gurnis*, 2008].

[22] Starting with the temperature field scaled from present-day tomography, we generate a first guess to the initial condition with a simple backward integration (SBI) of the forward model with gravity and plate motions reversed. This initial condition is subsequently updated according to a conjugate gradient algorithm

$$T_0^{i+1} = T_0^i - \gamma(i) \cdot \lambda_0^i \qquad (8)$$

where i is the iteration number and γ a damping factor. The iteration process terminates upon convergence of the cost function.

[23] We solve equations (2)–(4) and (7) with CitcomS, a finite element code for solving thermal convection [*Zhong et al.*, 2000]. Plate motions calculated at 1 Ma intervals and linearly interpolated for intervening times are used as boundary conditions. Other boundary conditions include an isothermal surface and an isothermal, free slip core mantle boundary. *Liu and Gurnis* [2008] developed an adjoint version by modifications of CitcomS Version 2.0, obtained from the Computational Infrastructure for Geodynamics (http://geodynamics.org).

[24] We use global flow models to avoid artifacts associated with imposed vertical boundaries. Our global model uses 12 caps with 129 × 129 nodes in each cap (approximately 40 km resolution in map view) and 65 grid points in radial direction. We also designed a regional model that covers a domain twice as wide (east-west) as NAM plate, allowing the plate to move since 100 Ma with all observations remaining >1,000 km from the vertical boundaries. The reflecting side boundaries caused a lower mantle return flow restricting the horizontal motion and resulting in Farallon slab positioned further to the west in the Late Cretaceous compared to the global model, implying that only global models are suitable for this and similar studies.

4.2. Sedimentation Model

[25] The models are tested by comparing dynamic topography (predicted stratigraphy) against observations. The model dynamic topography is rotated into the plate frame of reference [*Gurnis et al.*, 1998]. During the initial step (100 Ma), we assume an initial topography to which we add computed dynamic topography; defining the initial shape of basins and topographic highs. We impose eustasy based on published curves initially $SL(t_0)$, assuming marine deposition with constant rate (SR) in areas topographically lower than the water surface. The maximum sediment thickness Δz_S deposited during a time step, Δt, is:

$$\Delta z_S = SR \cdot \Delta t \qquad (9)$$

SR, 50 m/Ma (Table 1), is determined from the total long-wavelength thickness of Late Cretaceous isopach [*Cook and Bally*, 1975]. Since the ratio between geoid and dynamic topography is small, we assume a flat water surface [*Gurnis*, 1991]. We

assume uniform thickness of sediments across the basin. If the accommodation is less than allowed isostatically, we only fill to the maximum allowed value. We correct for Airy isostasy at the end of each time step:

$$d = Dz_S \cdot \frac{r_S - r_W}{r_M - r_W} \quad (10)$$

where d is basin depth correction, r_S, r_W and r_M are density of sediments (2,300 kg/m^3), water (1,000 kg/m^3), and mantle (3,300 kg/m^3), respectively. Isostatically adjusted topography becomes the input into each subsequent time step. For steps 1 to n we add the differential dynamic topography between steps n and $n - 1$, account for eustatic sea level change $SL(t_n)$, deposit sediments, and apply the isostatic adjustment, until we reach the final time step at 0 Ma.

[26] At each time step, we predict shoreline position as the 0 m contour and track dynamic topography at the position of each borehole. Cumulative Late Cretaceous isopach thickness is calculated as accumulated sediment thickness 100 to 65 Ma, with sediment compaction being neglected. Following the inference of mantle properties, we will determine the influence which initial NAM topography and eustatic sea level have on the stratigraphic predictions.

4.3. Constraining Mantle Properties

[27] The effective temperature scaling and mantle viscosities are treated as free variables that we attempt to constrain with dynamic topography and its rate of change, with relations following from the conservation of momentum and energy (equations (3) and (4)):

$$h = C_1 T_e \quad (11)$$

$$\dot{h} = \frac{C_2}{h_{um}} h_1^2 \quad (12)$$

where h is dynamic topography and $\dot{h}$ its rate of change; C_1 and C_2 are numerical constants obtained from the solution of flow and are dependent on the viscosity and temperature structure [*Gurnis et al.*, 2000]. Derivation and recovery of mantle properties with synthetic data are given by *Liu and Gurnis* [2008].

[28] We use two steps to constrain mantle properties. First the scaling between the magnitude of seismic anomalies and effective temperature is inferred, followed by the estimation of mantle viscosities. For a given thermal anomaly (density) in the upper mantle, equation (11) implies that the magnitude of surface dynamic topography is linearly related to the amplitude of thermal anomalies. This relation is not always valid since dynamic topography depends on the ratio of upper/lower mantle viscosity, but it is a good approximation for active subduction [cf. *Richards and Hager*, 1984]. For Farallon subduction, the modeled dynamic topography is associated with Cretaceous flooding over a lateral scale >1,000 km which, as we will show, requires the slab to be shallow and flat-lying, and thus enabling a constraint on the amplitude of T_e (equation (11)).

[29] The upper mantle viscosity is inversely proportional to the rate of change of dynamic topography [*Liu and Gurnis*, 2008, equation 10], which is constrained from stratigraphic data. Temporal evolution of flooding (shown by paleoshorelines) including its sudden appearance in the Late Albian and gradual demise in the Late Cretaceous provide constraints on mantle viscosity. Tectonic subsidence rate extracted from the boreholes is equivalent to the rate of change of dynamic topography in the NAM frame of reference.

4.4. Subduction Parameterization

[30] We started with simple models that include a 3 layer viscosity profile: a lithosphere with a viscosity of 5×10^{22} Pa s above 100 km depth, and an upper and lower mantle separated at 660 km with viscosities to be constrained. We also use a temperature-dependent viscosity, where a temperature decrease of 200□C results in an increase of viscosity by one order of magnitude.

[31] In the SBI the cold ''Farallon'' anomaly rises instead of sinks. By 70 Ma, within the upper mantle, the cold material diverges and partly deflects toward the east because of the reversely imposed plate motions (Figure 4a), resulting in geophysically unreasonable subduction inconsistent with the temporal sequence of subsidence and uplift of the WIS.

[32] In order to direct the Farallon slab toward the oceanic plate on the surface we implement a stress guide, a simple approach that couples the oceanic plate with the Farallon slab using the viscosity field. The implementation uses a high-viscosity layer (HVL) overlain by a low-viscosity channel (LVC) beneath the NAM plate [*Manea and Gurnis*, 2007; *Humphreys and Coblentz*, 2007] with one

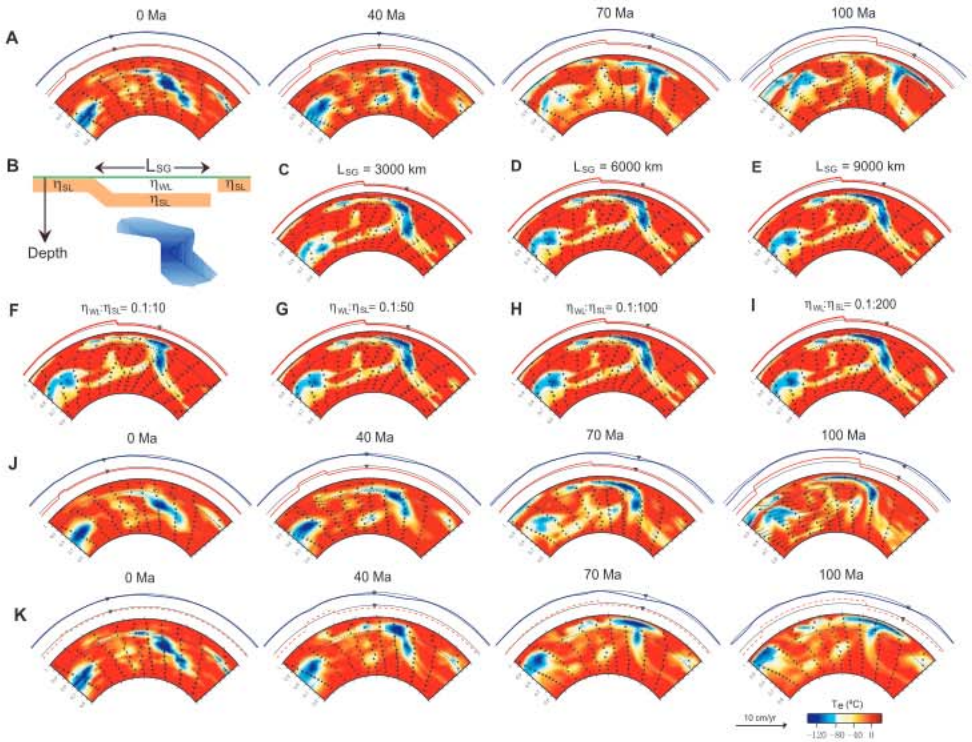

Figure 4. Subduction modeling with inverse method. All cross sections are at 41□N, with the velocity vectors (black arrows) plotted over the temperature field (in color). Dynamic topography (blue) and plate motions (red) along the profile are shown above the cross section. The black triangle denotes a borehole site (41.6□N, 254□E) that moves with the continent. All runs have a lower mantle viscosity $h_{LM} = 15$, $h_{UM} = 1$ and an effective temperature anomaly T_e = 160□C. (a) An SBI run with a standard model from present-day mantle structure leads to unrealistic subduction geometry back in time, indicating the requirement of a stress guide. (b) A sketch of the parameterized stress guide showing an imposed small viscosity (h_{WL}) layer overlying a large viscosity (h_{SL}) layer underneath the continent, where L_{SG} indicates the length of the guide. The recovered slab at 70 Ma (c–e) with the different values of L_{SG} and (f–i) with various viscosity ratios (relative to 10^{21} Pa s) within the two layers, showing the solutions converge as long as L_{SG} > 3,000 km and h_{WL}: h_{WL}< 0.1:50. (j) The evolution of the slab after five forward adjoint iterations including a stress guide with L_{SG} = 6,000 km and h_{WL}: h_{WL} = 0.1:100, where reasonable subduction geometry develops. (k) A free convection test showing that without the imposed plate motions and stress guide, the slab has almost the same vertical velocities as can be seen from the depth of the structure at different times.

end of the HVL attached to the oceanic plate at the trench (Figure 4b). The stress guide has a total thickness of 150 km. The recovery of the slab is almost identical in cases we explored as long as the stress guide is longer than 3,000 km (Figures 4c–4e), while the HVL with a viscosity larger than 5×10^{22} Pa s always produce nearly the same slab geometry (Figures 4f–4i). Imposed plate motion and the stress guide neither increases nor decreases the vertical velocities in models with plate motions (Figure 4a) or with both plate motions and the stress guide (Figure 4j), compared to those without imposed plate motions (Figure 4k). With such a stress guide, the adjoint method recovers the Farallon subduction while maintaining reasonable subduction geometry over time while reproducing the general characteristics of dynamic topography (Figure 4j) (as described below).

5. Results

5.1. Effective Temperature Anomaly

[33] Comparing model results with stratigraphy we attempt to bound three variables: upper mantle viscosity h_{UM}, lower mantle viscosity h_{LM} and the scaling G between seismic shear velocity anomaly and effective temperature T_e. Using a range of G (1×10^3, 2×10^3, 3×10^3□C/km/s) which give different effective temperature anomalies, we find that the recovered slabs will have nearly identical geometries if the lower mantle viscosity is compensated so that the effective Rayleigh number

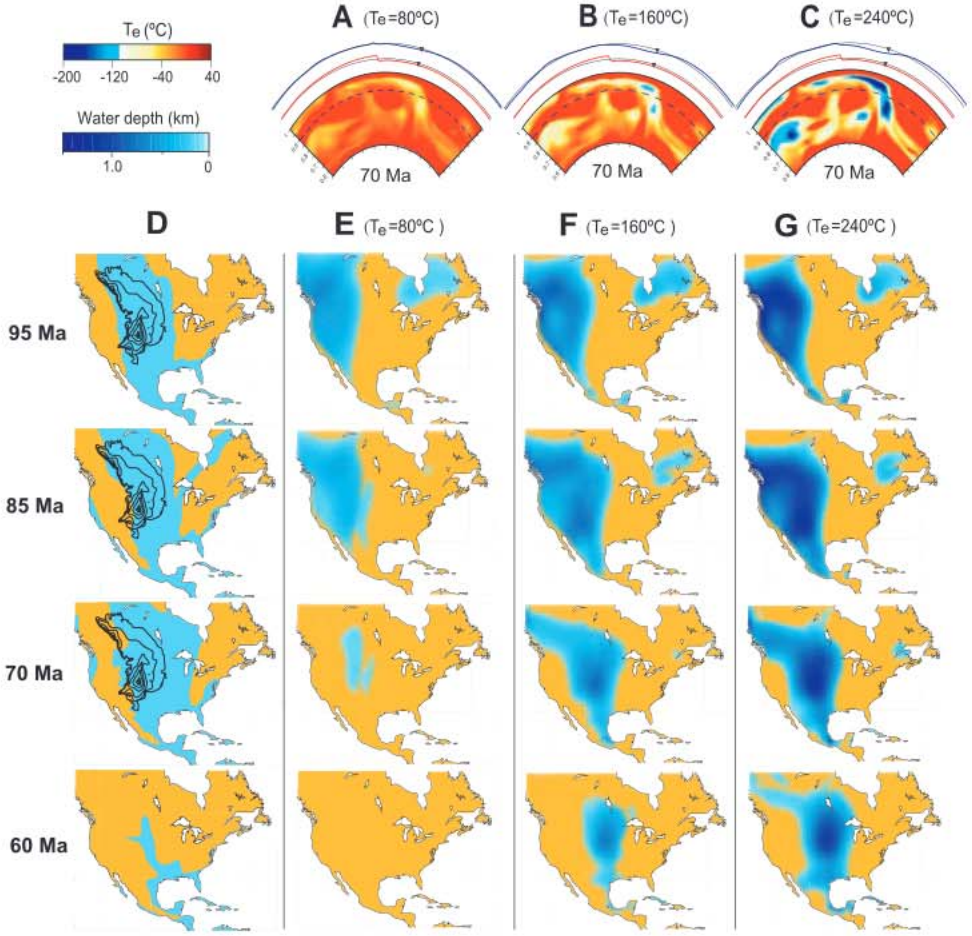

Figure 5. Selection of the effective temperature through flooding predictions. (a–c) Recovered Farallon slab at 70 Ma with three different magnitudes of temperature anomaly (80, 160, and 240□C, respectively) and lower mantle viscosities largely traded off with temperature (7×10^{21}, 15×10^{21}, and 30×10^{21} Pa s, respectively; all cases have an upper mantle viscosity of 10^{21} Pa s), where all three models see the same slab geometries. (d) Reconstructed WIS flooding (blue [*Smith et al.*, 1994]) and sediment isopachs (black contours with 2,000 ft contour interval [*Cook and Bally*, 1975]). (e–g) The predicted Late Cretaceous flooding with different T_e, with the 160□C temperature anomaly (Figure 5f) matching observations (Figure 5d) to the best extent.

remains invariant. In these cases, the convective velocities were nearly the same, except for small differences in the lateral variations in viscosity associated with temperature. Although the dynamic topography has the same spatial pattern, their magnitudes differ (Figures 5a–5c). Predicted flooding varies depending on dynamic subsidence: With an effective temperature anomaly of 80□C, the flooding occurs widely over the west at 95 Ma, but disappears soon after (Figure 5e); with a larger anomaly (240□C), the flooding is well correlated with WIS, but persists after the Cretaceous (Figure 5g); the flooding is well predicted with an anomaly of 160□C in both time and space (Figure 5f). The effective temperature scaling is about $G = 2 \times 10^3$□C/km/s, giving an effective temperature anomaly of 160□C. This value will be used in subsequent models.

5.2. Mantle Viscosities

[34] Once the effective temperature is constrained, upper and lower mantle viscosities can be retrieved from dynamic topography and its rate of change by comparing the fit to borehole tectonic subsidence and subsidence rate. We selected models with lower mantle viscosities h_{LM} between 1×10^{22} Pa s and 3×10^{22} Pa s and upper mantle viscosities h_{UM} between 0.1×10^{21} Pa s and 2×10^{21} Pa s, which are within the range of postglacial rebound-inferred values [*Milne et al.*, 2004; *Mitrovica and Forte*, 2004]. We tested models with lower mantle viscosities as high as 6×10^{22} Pa s, but these models yielded little or no flooding in the WIS.

[35] We calculated the RMS misfit (Figure 6) between tectonic subsidence and dynamic topog-

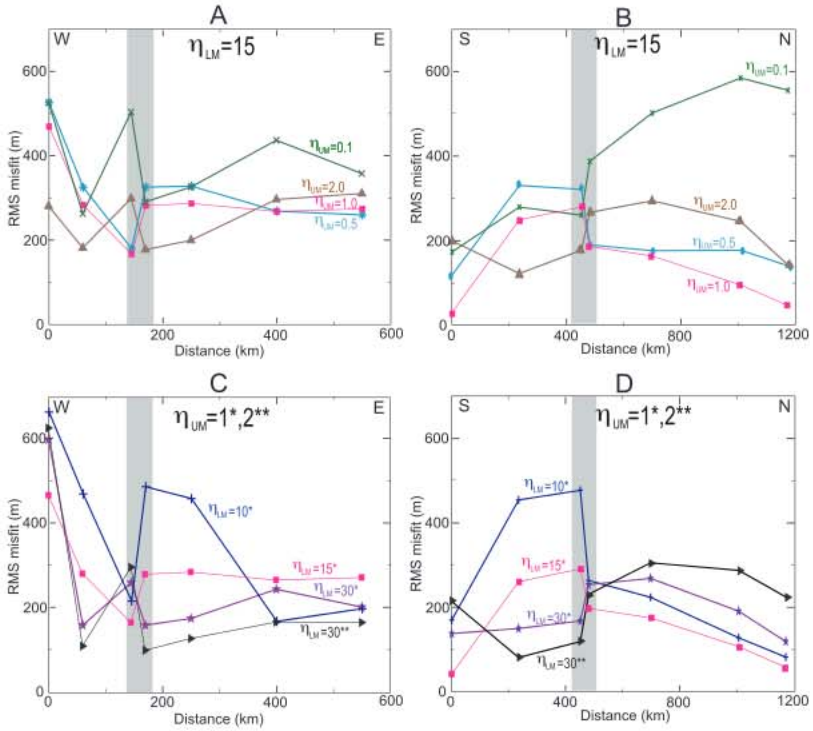

Figure 6. RMS amplitude misfit between observed and model borehole tectonic subsidence. (a and b) Misfit for models with constant lower mantle viscosity $h_{LM} = 1.5 \times 10^{22}$ Pa s. (c and d) Misfit for models with upper mantle viscosity $h_{LM} = 1–2 \times 10^{21}$ Pa s. Grey vertical bar indicates intersection of N-S and E-W profiles. All viscosity values are shown with respect to reference viscosity of 10^{21} Pa s.

raphy for each WIS borehole (Figure 1). While holding $h_{LM} = 1.5 \times 10^{22}$ Pa s fixed, the largest misfit for borehole subsidence is found for the smallest upper mantle viscosity, $h_{UM} = 0.1 \times 10^{21}$ Pa s (Figures 6a and 6b) because the model subsidence is too large at the beginning of the Late Cretaceous and too small from 70 to 60 Ma. A larger upper mantle viscosity provides a better fit: Along the E-W line (Figure 6a), a model with $h_{UM} = 2 \times 10^{21}$ Pa s provides the best prediction, while for the N-S line (Figure 6b) $h_{UM} = 1 \times 10^{21}$ Pa s is the preferred value. Alternatively, by fixing $h_{UM} = 10^{21}$ Pa s, the largest misfits occur for the smallest lower mantle viscosity ($h_{LM} = 1 \times 10^{22}$ Pa s) (Figures 6c and 6d). Models with lower mantle viscosities between 1.5 and 3.0×10^{22} Pa s give borehole subsidence prediction with lower RMS misfits (Figures 6c and 6d). There is a general trend of the westernmost boreholes (Figures 6a and 6b) having under predicted subsidences, which could be related to proximity to the Sevier belt (Figure 1) and supercrustal loading, which we do not account for.

[36] Since change of dynamic topography constrains upper mantle viscosity, h_{UM} (equation (12)), we compare the slope of tectonic subsidence curves (subsidence rate) against model results (Figure 7) by fitting a linear trend to the modeled and observed subsidence. The agreement between model predictions and observation vary significantly from location to location at greater than the 95% confidence level, indicating that this may not be the most robust parameter for the selection of mantle viscosities. However, we can confidently eliminate certain models, and models with ratios of lower/upper mantle viscosity that are either too high or too low. Specifically, the model with $h_{LM}/h_{UM} = 30:1$ ($h_{LM} = 1.5 \times 10^{22}$ Pa s and $h_{UM} = 0.5 \times 10^{21}$ Pa s) (Figures 7a and 7b) and $h_{LM}/h_{UM} = 10:1$ ($h_{LM} = 1.0 \times 10^{22}$ Pa s and $h_{UM} = 1.0 \times 10^{21}$ Pa s) (Figures 7c and 7d) can both be eliminated on the basis of subsidence rate.

[37] On the basis of the RMS misfit of tectonic subsidence (Figure 6) and subsidence rate (Figure 7) alone, there is no clear "best model" that yields the most robust fit. We therefore summarize the boreholes fits individually (Table 2) to define models with overall consistency with data. A successful model (pluses in Table 2) selection is based on two criteria: the smallest RMS misfit and the smallest discrepancy between observed and model subsidence rate. Once summarized in this fashion,

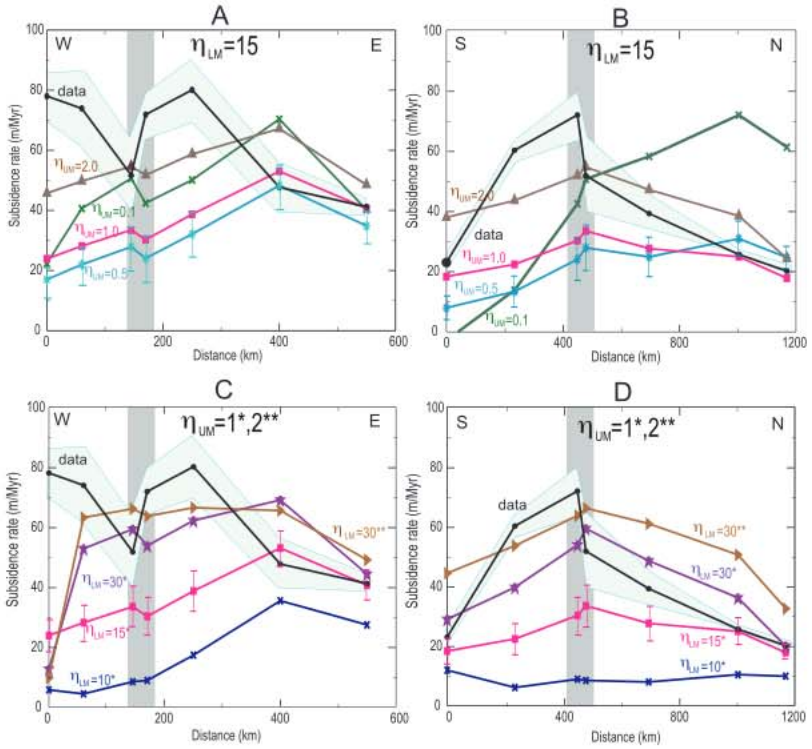

Figure 7. Comparison between observed and model subsidence rate. (a and b) Comparison for models with constant lower mantle viscosity $h_{LM} = 1.5 \times 10^{22}$ Pa s. (c and d) Comparison for models with upper mantle viscosity $h_{LM} = 1–2 \times 10^{21}$ Pa s. Observation (data) curve is shows with black line, and models are shown with colored lines. Light blue colored outline indicates 95% confidence interval for the observation, and colored bars indicate 95% confidence interval for a representative model, with all other models having similar confidence intervals. Grey vertical bar indicates area of intersection of N-S and E-W profiles. All viscosity values are shown with respect to reference viscosity of 10^{21} Pa s.

two models emerge (Table 2): (1) a model with $h_{LM} = 3 \times 10^{22}$ Pa s and $h_{UM} = 2 \times 10^{21}$ Pa s and (2) a model with $h_{LM} = 1.5 \times 10^{22}$ Pa s and $h_{UM} = 1 \times 10^{21}$ Pa. In addition, models with upper mantle viscosity smaller than 0.5×10^{21} Pa s never fit borehole subsidence satisfactorily (Table 2). Both models that yield good predictions of the borehole subsidence have lower/upper mantle viscosity ratio h_{LM}:h_{UM} = 15:1, suggesting that differential dynamic subsidence (with respect to 97 Ma) constrains ratio of upper/lower mantle viscosity. This tradeoff in absolute viscosities occurs within a limited range related to data uncertainties, i.e., the case with $h_{LM} = 6 \times 10^{22}$ Pa s and $h_{UM} = 4 \times 10^{21}$ Pa s is safely ruled out because the borehole subsidence rates are all underpredicted.

[38] The final selection of the preferred upper and lower mantle viscosities is based on the pattern of Cretaceous flooding. One of the best fitting models from borehole subsidence analysis ($h_{UM} = 10^{21}$ Pa s and $h_{LM} = 1.5 \times 10^{22}$ Pa s) well predicts the flooding (Figure 8b) in terms of the position of WIS between 85 and 60 Ma (Figures 8a and 8b), with individual borehole tectonic subsidence also being well predicted (Figures 8g–8i). Decreasing h_{UM} to 3×10^{20} Pa s (Figure 8c) and further to 10^{20} Pa s (Figure 8d) results in eastward and northward migration of flooding from 95 to 70 Ma, which is different from observations, where the flooding remains in the same location through the Late Cretaceous (Figure 8a). Smaller h_{UM} values lead to insufficient flooding at 95 Ma and excess flooding at 60 Ma (Figures 8c and 8d). Out of two models with the best predictions of the borehole subsidence, the model with $h_{UM} = 10^{21}$ Pa s and $h_{LM} = 1.5 \times 10^{22}$ Pa s gives the best predictions of the Cretaceous flooding and subsequent withdrawal of the interior seaway (Figure 8b). The model with $h_{UM} = 2 \times 10^{21}$ Pa s and $h_{LM} = 3.0 \times 10^{22}$ Pa s predicts flooding at 95 Ma and 85 Ma too far to the west (Figure 8e), and predicts a withdrawal of the interior seaway around 70 Ma, too early compared to the paleogeographic reconstructions. The preferred model with $h_{UM} = 10^{21}$ Pa s and $h_{LM} = 1.5 \times 10^{22}$ Pa s (Figure 8b) predicts flooding that is too far to the west only at 95 Ma,

Table 2. Summary of Misfits Between Observed and Model Tectonic Subsidence Based on RMS Amplitude and Subsidence Rate Criteria[a]

			EW Line						NS Line						
h_{LM}	h_{UM}	Criteria	1	2	3	4	5	6	1	2	3	4	5	6	Total[b]
10	1	Slope									+				2
		RMS					+								
15	0.1	Slope													0
		RMS													
15	0.3	Slope													0
		RMS													
15	0.5	Slope					+								1
		RMS													
15	1	Slope						+	+				+		8
		RMS							+		+	+	+	+	
15	1.5	Slope										+			1
		RMS													
15	2	Slope	+												2
		RMS	+												
20	0.3	Slope													0
		RMS													
30	1	Slope												+	1
		RMS													
30	2	Slope		+	+	+				+					9
		RMS		+	+	+		+		+					

[a] For each well, we evaluated the model with the smallest misfits based on two criteria and marked it with a plus. Values of upper mantle viscosity h_{UM} and lower mantle viscosity h_{LM} are given with respect to reference value of 10^{21} Pa s.
[b] Total includes both slope and RMS criteria for each well.

while the spatial localization of the flooding corresponds to paleogeographic reconstructions at all subsequent times.

[39] When the descent of the Farallon anomaly is reversed from its present-day depth to the surface, the structure traverses a much longer path through the lower mantle compared to the upper mantle. Thus, the lower mantle viscosity largely controls the timing and position of flat slab formation during Farallon subduction, and the position and timing of Late Cretaceous flooding. When the lower mantle viscosity is 3×10^{22} Pa s (Figure 8e), the slab remains in the lower mantle for a longer duration leading to a smaller magnitude of dynamic topography at 70 Ma with little flooding (Figure 8e). A smaller lower mantle viscosity (10^{22} Pa s) allows the slab to stay in the upper mantle longer, and this leads to sustained flooding over an unreasonably large area throughout the Late Cretaceous (Figure 8f). Another aspect is the extent of the flat slab underneath the continent (Figure 4j): The slab stays for a longer (shorter) period in a higher- (lower-) viscosity lower mantle, so the flat subduction has a smaller (larger) spatial extent as the overriding plate moves toward the west at a given velocity. This is reflected in the position of flooding, where a lower mantle with a higher viscosity (Figure 8e) shows a westward shift of flooding, and that with a lower viscosity (Figure 8f) shows an eastward shift, compared to intermediate value of lower mantle viscosity (Figure 8b).

5.3. Influence of Eustasy and Initial Topography on Model Predictions

[40] Since the assumed eustatic curve may influence our results, we explored the sensitivity of this assumption using our preferred mantle viscosity model ($h_{UM} = 1 \times 10^{21}$ Pa s, $h_{LM} = 1.5 \times 10^{22}$ Pa s) (Figure 9). When we impose no eustatic change (Figure 9b) or the *Miller et al.* [2005] sea level curve (Figure 9c), we predict less widespread flooding, comparing to one using the *Haq et al.* [1987] or *Müller et al.* [2008b] curves (Figures 9d and 9e). Initially (at 95 Ma), by imposing small sea levels, we produce a narrower epicontinental sea and more constrained flooding north-south (Figures 9b and 9c), compared with predictions using significantly higher (Figures 9d and 9e) Late Cretaceous sea levels. At 85 and 70 Ma, we predict wider flooding east-west when we impose *Haq and Al-Qahtani* [2005] or *Müller et al.* [2008b] sea levels. All cases predict reduced extents of flooding at 60 Ma compared to 95, 80 and 70 Ma, consistent with overall withdrawal of the interior seaway at the end of Cretaceous. However, in all cases (Figures 9b–9e) we still predict widespread flood-

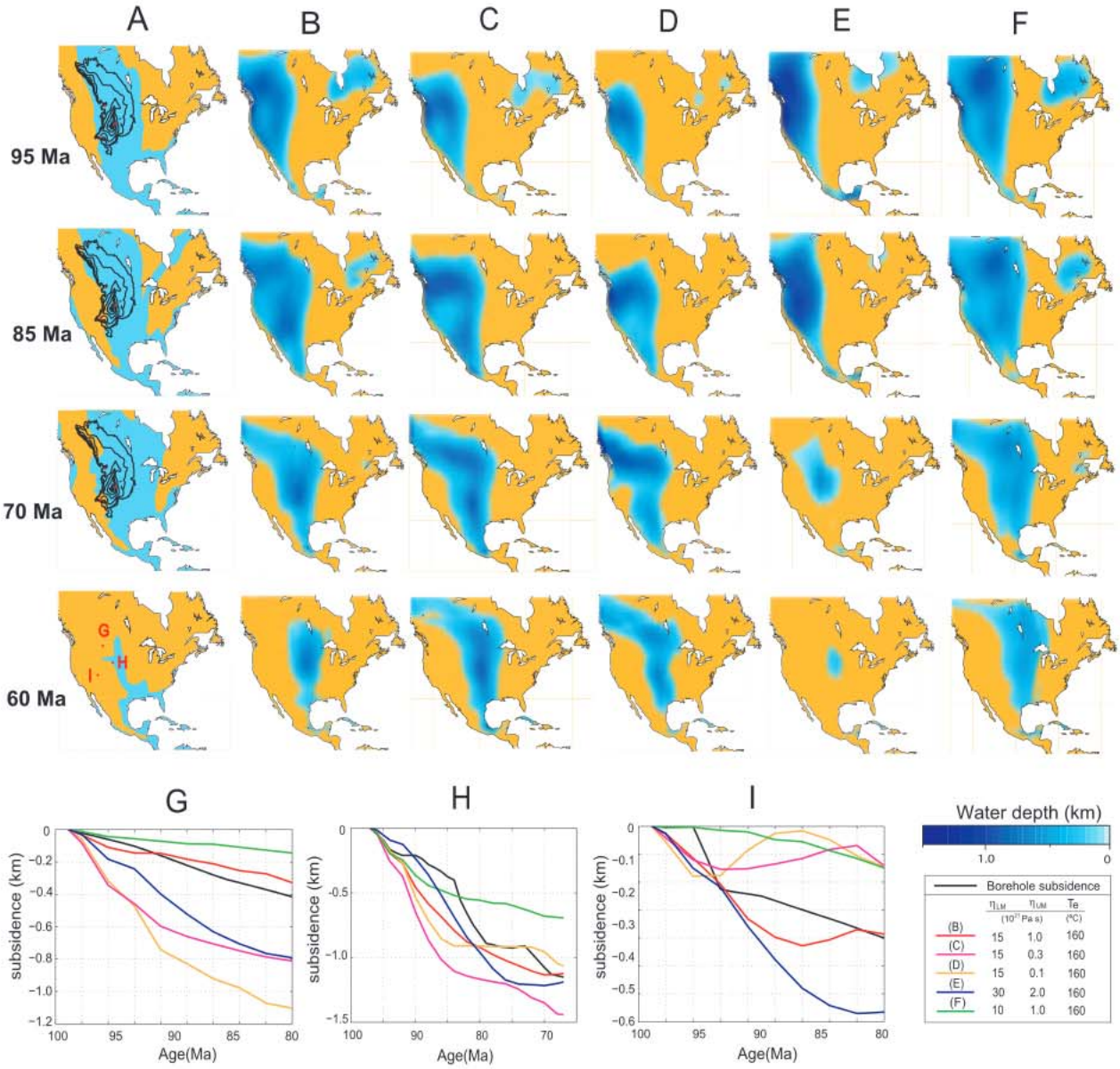

Figure 8. Effects of mantle viscosities on flooding predictions and borehole subsidence. (a) Observed flooding [*Smith et al.*, 1994]. (b–f) Predicted flooding with different models (parameters are given in the bottom right corner; viscosities relative to10^{21} Pa s). (g–i) Borehole subsidence predictions (colored lines) compared to observations (black line).

ing during Cretaceous and subsequent early Cenozoic withdrawal. Different sea levels give minor differences in flooding patterns, implying that dynamic topography represents a primary control of long-wavelength Late Cretaceous marine inundation within the interior of NAM, and that eustasy is maybe secondary.

[41] Our flooding model starts with a given initial topography and plays a significant role in the overall results. Since little knowledge exists on NAM topography during the Late Cretaceous, we used several alternative initial topographies: A flat Earth (Figure 10b), present-day (Figure 10c), present-day scaled by 0.5 (Figure 10d), and present-day with Cretaceous sediments isostatically removed (Figure 10e). To maximize flooding estimates, we applied the *Haq and Al-Qahtani* [2005] curve. A model with an initially flat surface (Figure 10b) predicts a pattern and duration closest to the observed (Figure 10b). When initialized with the present-day topography, we obtain little flooding (Figure 10c), even with the high-amplitude eustasy. Similarly, when we use half value of the present-day topography (Figure 10d) or that modified by

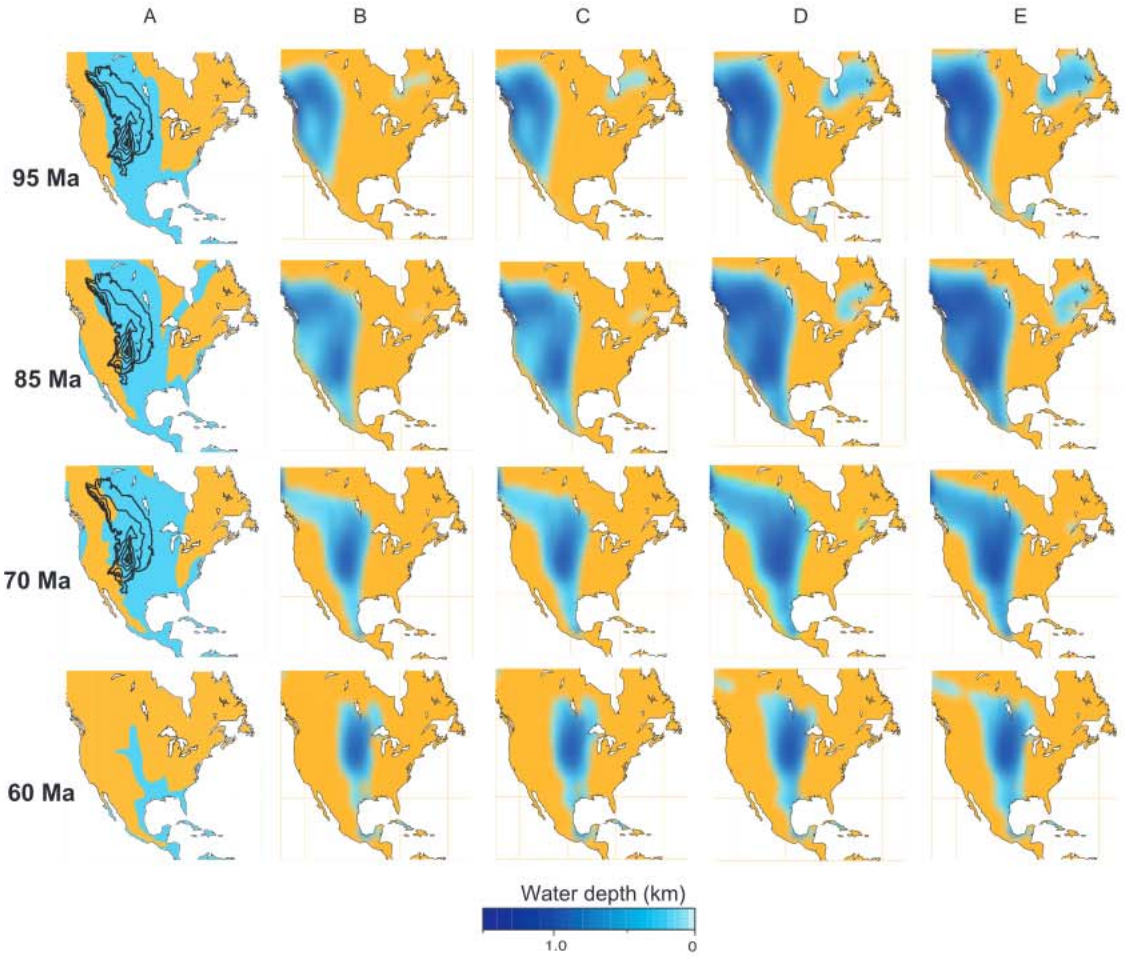

Figure 9. Effect of eustasy on predicted flooding. (a) Reconstructed flooding (blue [*Smith et al.*, 1994]). (b) Prediction with no change in sea level. (C) Prediction using *Miller et al.* [2005] sea level. (d) Prediction using *Müller et al.* [2008b] sea level. (e) Prediction using *Haq and Al-Qahtani* [2005] sea level. Black contours show Late Cretaceous isopach [*Cook and Bally*, 1975] with 2000 ft contour interval. All predictions are using initially flat Earth topography.

removal sediments (Figure 10e), we still under predict Cretaceous flooding.

5.4. Dynamic Subsidence of the U.S. East Coast

[42] Presently, the Farallon slab is imaged in the midmantle under the U.S. east coast (Figure 2), creating a long-wavelength small-amplitude dynamic topography low. *Spasojević et al.* [2008] analyzed Eocene and Miocene paleoshorelines, suggesting at least 50 m, and probably as much as 200 m of dynamic subsidence since the Eocene (Figure 11), consistent with the discrepancy between regional and global sea level. Similarly, *Conrad et al.* [2004] predict a modeled dynamic topography low on the east coast from the Farallon slab, while *Moucha et al.* [2008] suggested that the same region is not a stable reference frame because of the effect of time-dependent dynamic topography.

[43] All models that we explored, predict Tertiary subsidence of the U.S. east coast (Figure 11). Models that yielded the best fits to WIS borehole subsidence (Figure 11, cases 2–3) predict 700–900 m subsidence since the early Eocene, and 250 m since the early Miocene. Models scaling both positive and negative S wave anomalies (Figure 11, case 1) yield the largest estimate of post Eocene subsidence. These models (Figure 11, cases 1–3) overestimate the amount of subsidence, compared with paleoshorelines and sea level discrepancies.

[44] In order to reduce dynamic subsidence since 55 Ma, we introduce an additional viscosity layer in the uppermost mantle that was not required to fit Late Cretaceous flooding and subsidence. This layer extends from the base of the lithosphere to 410 km

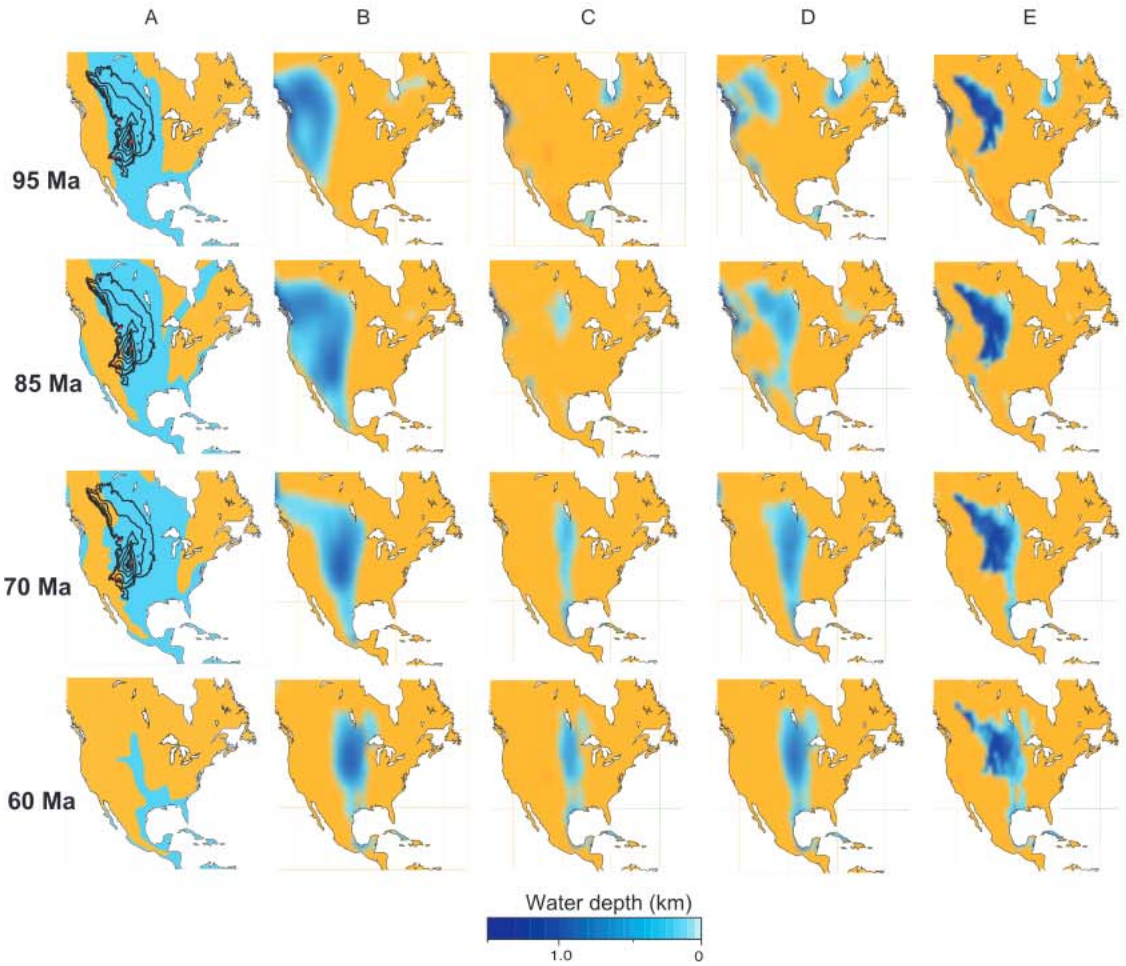

Figure 10. Effect of initial topography on predicted flooding. (a) Reconstructed flooding (blue [*Smith et al.*, 1994]). (b) Prediction using initially flat Earth topography. (c) Prediction using present-day North America topography. (d) Prediction using present-day North America topography multiplied by 0.5. (e) Prediction using present-day topography with Cretaceous sediments isostatically removed. Black contours show Late Cretaceous isopach [*Cook and Bally*, 1975] with 2,000 ft contour interval. All predictions are using *Haq and Al-Qahtani* [2005] sea level.

depth with a viscosity of 10^{20} Pa s, while the transition zone has a viscosity of 10^{21} Pa s. Estimates of dynamic subsidence since the early Eocene for this four-layer mantle are 480–560 m (Figure 11, cases 4–5), consistent with subsidence estimates based on paleoshorelines and sea level discrepancies. Models with an additional layer in the upper mantle yield the same Late Cretaceous subsidence and flooding as the three-layer models, given that lower mantle viscosity is the same in both three- and four-layer models, and that upper mantle viscosity in the three-layer model is the same as transition zone viscosity in the four-layer model.

6. Discussion and Conclusions

[45] The results presented here were obtained using adjoint convection models for the evolution of the Farallon slab since the Late Cretaceous, constrained by seismic tomography and plate motions. The algorithm implements an optimal first guess to the initial condition, temperature-dependent viscosity, and it is constrained by time-dependent and spatially dependent stratigraphic data. A simple correlation between NAM Cretaceous stratigraphy and seismic tomography shows that Late Cretaceous total isopach correlates well with present-day remnants of the Farallon slab with maximum correlation at depths 1,500–1,700 km. The maximum correlation between large seismic velocities anomalies, presumed to represent the Farallon remnants, and Late Cretaceous isopach rotated in the mantle frame of reference, occurs at a depth of 1,525 km for a rotation to 80 Ma and 1,675 km to 100 Ma. The average descent velocity of the Farallon slab back to 100 Ma and 80 Ma are 1.6 and 1.8 cm/a, respectively. The smaller of the two velocities

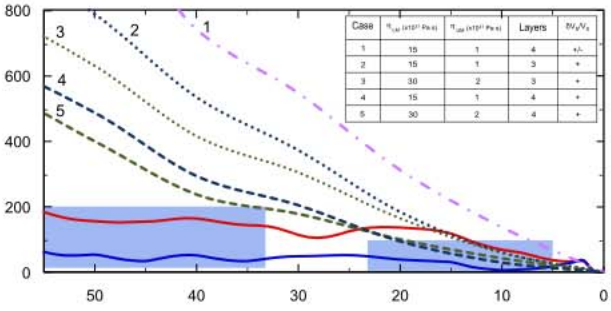

Figure 11. Predictions of the U.S. east coast subsidence. Dynamic topography change for a well in New Jersey coastal plain (coordinates 74□30′W, 39□30′N) for five dynamic models is shown with colored dotted and dashed lines. Solid red and blue lines show difference between sea level models of *Haq and Al-Qahtani* [2005] and *Miller et al.* [2005] and *Kominz* [1984] and *Miller et al.* [2005], respectively. Blue colored boxes show estimated subsidence range from paleoshoreline analysis for Eocene and Miocene. Inset shows model parameters (h, viscosity; LM, lower mantle; UM, upper mantle viscosity; dV_S/V_S, seismic anomaly with positive (+) or both positive and negative (±) signals included). Dynamic topography was calculated as if were an interface between mantle and water.

averaged over the longer time period implies that the Farallon slab has a slower vertical speed in its early stage of subduction between 100 and 80 Ma. The rather fast convergence of the Farallon and NAM plates during this time, therefore, suggests that the Farallon plate must have been moving faster laterally than vertically, consistent with flat subduction epoch [e.g., *Saleeby*, 2003].

[46] In order to obtain reasonable subduction geometry, we parameterized a stress guide. By computing a range of cases in which the thickness, length, and strength of the guide were varied, we found that the onset of flat lying subduction was not strongly affected by stress guide details as long as one was incorporated. The variation in upper and lower mantle viscosity and seismic scaling had a larger influence. How slabs are represented can be improved. First, seismic models showing the connection of the Juan de Fuca slab to the Farallon anomaly are improving [e.g., *Roth et al.*, 2008]. This should allow one to use a purely seismic-based approach to define present structure. Second, forward models incorporating realistic rheologies are improving [*Billen*, 2008], and so higher-resolution methods will eventually be used in inversions as improvements in hardware and software allow.

[47] We attempt to infer upper and lower mantle viscosities iteratively with stratigraphic constraints. The misfit with observed subsidence and its rate of change allow us to narrow the range of viscosities, with the preferred values primarily based on flooding. Our preferred viscosity model has an upper mantle viscosity of 1×10^{21} Pa s, and a lower mantle viscosity of 1.5×10^{22} Pa s. These represent background viscosities locally modified by the Farallon slab. Consequently, the average profiles inferred from post glacial rebound and the present-day geoid are more complex in depth [*Mitrovica and Forte*, 2004] than ours. Thus, the ratio of mantle viscosities across 660 km discontinuity in our preferred model is 15:1, slightly smaller than the factor of 30 or more suggested using the geoid as a constraint on instantaneous flow models [*Hager*, 1984; *King and Masters*, 1992]. However, the values we propose for effective viscosities under NAM are within the range proposed through studies of postglacial isostatic adjustment. *Milne et al.* [2004] define range of upper mantle viscosities between 5×10^{20} Pa s and 10^{21} Pa s, and lower mantle viscosities between 5×10^{21} Pa s and 5×10^{22} Pa s. Comparing to the values proposed by joint inversion of convection and glacial isostatic adjustment data [*Mitrovica and Forte*, 2004], our effective upper mantle viscosity is equivalent to the value proposed for the bottom of the upper mantle and top of the lower mantle, while the proposed lower mantle viscosity has the same value as the one defined by *Mitrovica and Forte* [2004] for the depth range of roughly 2,200–2,500 km.

[48] Downwelling associated with subduction of the Farallon slab creates a dynamic topography low in the western interior during Cretaceous (Figure 12b). The dynamic topography low migrates eastward from 100 Ma to the present in the NAM frame of reference. Over the Late Cretaceous, the dynamic topography low has the largest amplitude (up to 1.5 km), and is located in the area of WIS. This dynamic topography low is inundated by epicontinental seas, resulting in widespread Cretaceous flooding (Figure 12c). Since there is disagreement between different authors on the amplitude of the global sea level since the Late Cretaceous, we model Cretaceous flooding with different sea level curves [*Miller et al.*, 2005; *Müller et al.*, 2008b; *Haq and Al-Qahtani*, 2005]. We obtain flooding patterns that match long-wavelength features of shorelines that vary in amplitude from 0 to 250 m depending on the assumed eustasy (Figure 9). On the basis of the analysis of observed sediment thickness and eustatic sea level, *Bond* [1976] also proposed that North America experienced significant continental

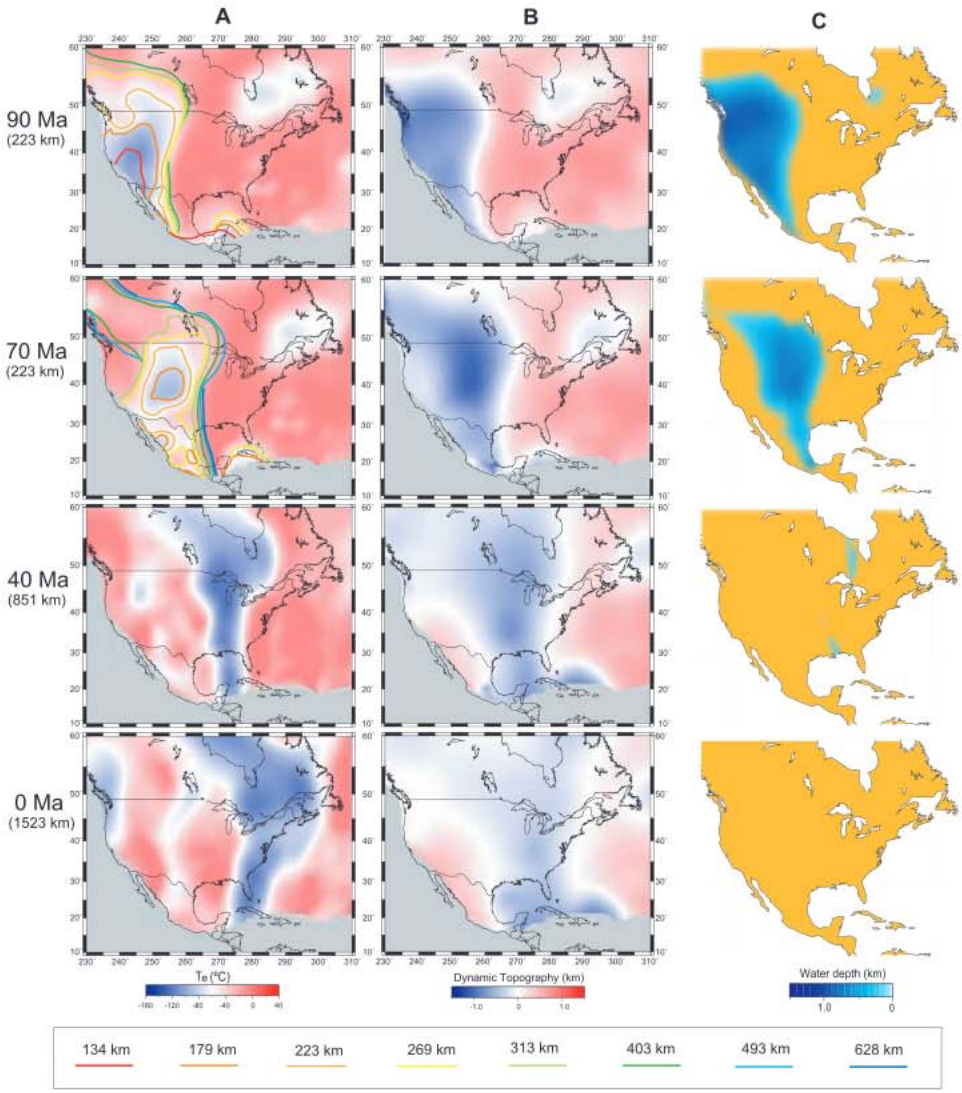

Figure 12. Evolution of the Farallon plate subduction viewed in the NAM reference frame. This model has a viscosity of the upper mantle at 10^{20} Pa s, of the transition zone at 10^{21} Pa s, and of the lower mantle at 1.5×10^{22} Pa s and an effective temperature anomaly of 160□C. (a) Slab geometries at different depth, where the background color represent the temperature field at depth denoted at the left margin and color contours show boundaries of the slab at different depths. (b) The associated surface dynamic topography. (c) Predicted continental flooding at different geological times using initially flat continent at 100 Ma and *Haq and Al-Qahtani* [2005] sea level.

submergence. The long-wavelength dynamic subsidence on order of 1,500 km was attributed to subduction of the Farallon slab [*Mitrovica et al.*, 1989; *Liu et al.*, 2005; *Liu and Nummedal*, 2004]. However, our results suggest that the first-order flooding patterns of the WIS is controlled primarily by long-wavelength dynamic topography attributed to the subduction of the Farallon slab, with eustasy playing a smaller role. Short-wavelength flexural loading component that changes on the time scale of a few million years has been attributed to the loading of the thrust belt [*Liu and Nummedal*, 2004], not accounted for in our models. However, this component probably plays an important role for controlling sediment deposition on short length scales over hundreds of km [*Currie*, 2002], and it is not a primary factor affecting long-wavelength flooding.

[49] As the Farallon slab continues sinking under the continent during Cenozoic, NAM moves westward in the mantle reference frame over this downwelling. A dynamic topography low, therefore, moves eastward in the NAM frame of reference. At 40 Ma (Figure 12b) the dynamic topography low is located under the central portions of the continent, while at the present day the dynamic topography low is located under the U.S. east coast

(Figure 12b). As the locus of dynamic topography moves eastward from WIS at the end of Cretaceous, flooding is reduced and the interior seaway eventually vanishes, and no significant flooding is developed in the interior of the NAM during Cenozoic, as suggested by paleogeographic reconstructions [*Smith et al.*, 1994]. A region of high dynamic topography subsequently develops in the western North America during the Cenozoic, contributing to the overall uplift of the region previously located in WIS. The Laramide orogeny started in the Late Cretaceous, 70 to 80 Ma ago [*Bird*, 1998], and ended 35 to 55 Ma ago, although the exact timing is under discussion [*English and Johnston*, 2004]. The region affected by the orogeny extends from Alaska to northern Mexico, forming the Rocky Mountain fold-and-thrust belt in Canada and the United States, and the Sierra Madre Oriental fold-and-thrust belt in east-central Mexico [*English and Johnston*, 2004]. Dynamic effects of flat slab subduction have been suggested as one of possible driving mechanisms for Laramide uplift [*English and Johnston*, 2004], along with other mechanisms such as retroarc thrusting, effects of Cordillerean collision [*English and Johnston*, 2004], or crustal processes (such as horizontal shortening, magmatic injection or lower crust displacement) or partial delamination of the lithosphere [*McQuarrie and Chase*, 2000]. *Mitrovica et al.* [1989] proposed that the interior of NAM rebounds and uplifts after convergence slows down or ceases because of the detachment of the slab or accretion of a terrane. Our model predicts a continuous contribution of high dynamic topography to the overall uplift of the region once occupied by the WIS since the end of Late Cretaceous.

[50] *Heller et al.* [2003] analyzed widespread conglomeratic units that were deposited in Mesozoic and Cenozoic over large length scales in NAM, recording regional tilts of the continent, associated with 400–800 m of differential uplift on areas as wide as 800 km and in time periods of 1 to 10 Ma. Westward movement of the plate in the mantle frame of reference over a downwelling created by Farallon slab subduction and associated change of dynamic topography (Figure 12b) provides a dynamic model that could potentially explain tilting of sedimentary units, such as gravel deposits overlying the Morrison Formation in the Rocky Mountains [*Heller et al.*, 2003] and gravel-rich Ogallala Group of Miocene-Pliocene age in Western Nebraska and southern Wyoming. *Heller et al.* [2003] suggest that rarity of preserved evidence of the widespread units could be attributed to either low preservation potential of the conglomeratic units or relatively unusual episodes of tilting. Our model suggests that the tilting due to development of differential dynamic uplift should be a continuous process. Thus, the absence of more geological evidence of the widespread conglomeratic units [*Heller et al.*, 2003] could be related to limited preservation potential in an environment that is continuously uplifting and being exposed to erosion.

[51] Presently, the dynamic topography low is located under the east coast, and all models we computed predict overall subsidence during the Cenozoic. The accumulated subsidence on the east coast due to the sinking of the Farallon slab remnant during the Cenozoic is on the order of 500 m, with approximately 250 m of subsidence occurring since the end of Eocene. Analysis of Eocene and Miocene paleoshorelines indicates that these paleoshorelines have present-day elevations 50–200 m lower than respective sea levels in these time intervals, which is consistent with the overall subsidence of the east coast [*Spasojevic et al.*, 2008]. The proposed dynamic subsidence can possibly explain the discrepancy between the *Miller et al.* [2005] sea level curve and other eustatic curves [*Spasojevic et al.*, 2008]. Geodynamically, the region of the U.S. east coast is not stable over longer time scales because of the sinking of the Farallon slab and should not be used as a type-locality when determining global sea level curves, as also suggested by others [*Moucha et al.*, 2008; *Müller et al.*, 2008b].

[52] We fit a wide range of Late Cretaceous stratigraphy in an adjoint model with a simple viscosity structure, including fewer layers than sometime used [e.g., *Mitrovica and Forte*, 2004]. However, to obtain more realistic amplitudes of dynamic subsidence on the U.S. east coast, our model requires an introduction of an additional low-viscosity layer below the lithosphere, with a viscosity of 1×10^{20} Pa s. Models with this extra layer of low-viscosity upper mantle produce the same patterns of Late Cretaceous flooding (Figure 12c) and subsidence as those without (Figure 8b). This indicates that more layers of mantle radial viscosity structure can be inferred when incorporating constraints over a larger time scale. Our scheme for constraining upper and lower mantle viscosities using stratigraphy combines quantitative and qualitative criteria iteratively. In the future, as databases with stratigraphic data are expanded, and as adjoint modeling capabilities and tomography models are improved, it may be possible to develop a fully automated scheme that iteratively updates mantle structure.

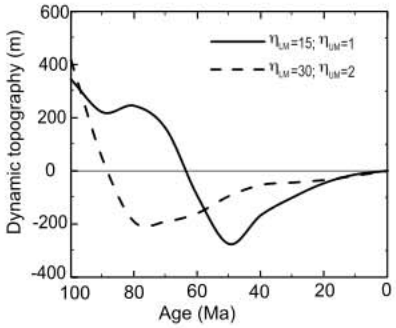

Figure 13. Time-dependent predictions of dynamic subsidence for East Lake Athabasca region (coordinates 108□W, 59□15′N) for two dynamic models. Values of upper mantle viscosity h_{UM} and lower mantle viscosity h_{LM} are given with respect to reference value of 10^{21} Pa s.

[53] Predictions of Cretaceous flooding from model dynamic topography are dependent on the assumption of initial topography of NAM. When we use present-day topography, we cannot predict any significant flooding of the western interior over the Cretaceous, even when we impose the highest proposed eustatic sea levels [*Haq and Al-Qahtani*, 2005] since 100 Ma. The widespread Cretaceous flooding [*Sloss*, 1988; *Smith et al.*, 1994] can be reproduced from dynamic topography only when initial topography was flat or with a gentle relief. This implies that the Late Cretaceous topography was very different from the present day, where most of the western portions of the continent, especially the region once occupied by WIS, was probably low lying at 100 Ma. This is consistent with previous inferences since a significant part of the continent has been uplifted since 70–80 Ma [*McMillan et al.*, 2006; *English and Johnston*, 2004; *Mitrovica et al.*, 1989] and this uplift has been especially significant in the western interior. However, the details of paleoelevation of the WIS are controversial. Structural and unroofing history studies of the Laramide mountains suggest that 1.5–3 km of relief was produced during Paleocene and early Eocene [*DeCelles et al.*, 1991]. This is supported by $d^{18}O$ analysis of apatite [*Fricke*, 2003], which suggests that the Laramide mountain regional paleoelevation in Wyoming in the early Eocene was on the order of 475 m, and that most of the high present-day elevation developed since the early Eocene. *Dettman and Lohmann* [2000], on other hand, use the study of $d^{18}O$ of river waters from the Late Cretaceous and Paleogene basins of Alberta, Montana, Wyoming and Colorado using aragonite mollusk fossils, concluding that the estimated altitude difference of river profiles is similar to the present-day value, suggesting that WIS had significant paleoelevation [*Dettman and Lohmann*, 2000].

[54] The western Canadian shield (Figure 1) is located at the edge of the region of influence of Farallon subduction (Figure 12). In order to infer burial history, *Flowers* [2009] analyzes the role of radiation damage on apatite (U-Th)/He ages of basement samples on the Canadian shield (near East Lake Athabasca). She proposes that $\geq$ 1.0 km of late Paleozoic-Mesozoic strata were deposited in the East Lake Athabasca region, hundreds of kilometers east of the preserved extent of sediments of the same age. These sediments have presumably been subsequently removed during periods of uplift. In addition, on the basis of thermochronology, deposition of more than several hundred meters of sediments during Cretaceous was unlikely [*Flowers*, 2009]. Two models preferred by the analysis of the borehole subsidence in the WIS predict a total of 600 m of subsidence in Late Cretaceous–early Cenozoic in the East Lake Athabasca region, followed by subsequent uplift (Figure 13). The maximum depth of depression created because of dynamic topography is 280 m, assuming a flat initial topography. Accounting for isostasy, the maximum thickness of potentially deposited sediments is 650 m, if the whole surrounding region was at sea level. This value is similar to one proposed by *Flowers* [2009], indicating that dynamic models can be used in conjunction with thermochoronology to infer regions that have been inundated in the past, but where the sedimentary record has been subsequently removed.

[55] Our inverse dynamic models based on seismic tomography, reversed to the Late Cretaceous, show the formation of flat subduction associated with broad surface dynamic subsidence [*Liu et al.*, 2008]. The model best fitting Cretaceous stratigraphy displays a flat to shallow-dipping slab extending ~2,000 km inland at around 70 Ma (Figure 4b). By further attempting to fit the models to east coast subsidence, requires weaker upper mantle, but the evolution of the Farallon slab and associated Late Cretaceous dynamics remains similar (Figure 12) as in models with simpler vertical viscosity model (Figure 8). Our model reproduces a flat slab that correlates well with the region of basement cutting Laramide-type faults in the western U.S. from 80 to 65 Ma [*Saleeby*, 2003]. Beyond the flat slab, there is a vast zone of shallow dipping subduction that

extends more than 1,000 km eastward and northward especially from 90 to 70 Ma (Figure 12a). The zone is significantly larger than inferred from a simplified set of forward models that neither incorporated the details of subduction nor attempted to match stratigraphy [*Bunge and Grand*, 2000].

Acknowledgments

[56] We thank Jason Saleeby and Dietmar Müller for valuable discussions during the course of this work and Rhodri Davies and Dag Nummedal for helpful reviews. We thank Becky Flowers for sharing her work in advance of publication. This is contribution 10,012 of the Division of Geological and Planetary Sciences and contribution 95 of the Tectonics Observatory, Caltech. The original CitcomS software was obtained from Computational Infrastructure for Geodynamics (CIG) (http://geodynamics.org). All calculations carried out on the Caltech Geosciences Supercomputer Facility are partially supported by NSF EAR-0521699. This work was supported through the Caltech Tectonics Observatory (by the Gordon and Betty Moore Foundation), the National Science Foundation (EAR-0609707 and EAR-0810303), StatoilHydro, and an ExxonMobil Science grant (to S.S.).

References

Atwater, T., and J. M. Stock (1998), Pacific–North America plate tectonics of the Neogene Southwestern United States—An update, *Int. Geol. Rev.*, *40*, 375–402.

Billen, M. (2008), Modeling the dynamics of subducting slabs, *Annu. Rev. Earth Planet. Sci.*, *36*, 325–356, doi:10.1146/annurev.earth.36.031207.124129.

Bird, P. (1998), Kinematic history of the Laramide orogeny in latitudes 35□49□N, western United States, *Tectonics*, *17*, 780–801, doi:10.1029/98TC02698.

Bond, G. (1976), Evidence for continental subsidence in North America during the Late Cretaceous global submergence, *Geology*, *4*, 557–560, doi:10.1130/0091-7613(1976)4<557:EFCSIN>2.0.CO;2.

Bond, G. (1978), Speculations on real sea-level changes and vertical motions of continents at selected times in Cretaceous and Tertiary periods, *Geology*, *6*, 247–250, doi:10.1130/0091-7613(1978)6<247:SORSCA>2.0.CO;2.

Bond, G. C. (1979), Evidence for some uplifts of large magnitude in continental platforms, *Tectonophysics*, *61*, 285–305, doi:10.1016/0040-1951(79)90302-0.

Bunge, H.-P., and S. P. Grand (2000), Mesozoic plate-motion history below the northeast Pacific Ocean from seismic images of the subducted Farallon slab, *Nature*, *405*, 337–340, doi:10.1038/35012586.

Bunge, H.-P., C. R. Hagelberg, and B. J. Travis (2003), Mantle circulation models with variational data assimilation: Inferring past mantle flow and structure from plate motion histories and seismic tomography, *Geophys. J. Int.*, *152*(2), 280–301, doi:10.1046/j.1365-246X.2003.01823.x.

Burgess, P. M., M. Gurnis, and L. Moresi (1997), Formation of sequences in the cratonic interior of North America by interaction between mantle, eustatic and stratigraphic processes, *Geol. Soc. Am. Bull.*, *109*, 1515–1535, doi:10.1130/0016-7606(1997)109<1515:FOSITC>2.3.CO;2.

Conrad, C. P., and L. Husson (2009), Influence of dynamic topography on sea level and its rate of change, *Lithosphere*, in press.

Conrad, C. P., C. Lithgow-Bertelloni, and K. E. Louden (2004), Iceland, the Farallon slab, and dynamic topography of the North Atlantic, *Geology*, *32*, 177–180, doi:10.1130/G20137.1.

Cook, T. D., and A. W. Bally (1975), *Stratigraphic Atlas of North and Central America*, 272 pp., Princeton Univ. Press, Princeton, N. J.

Cross, T. A., and R. H. Pilger, Jr. (1978), Tectonic controls of late Cretaceous sedimentation, western interior, USA, *Nature*, *274*, 653–657, doi:10.1038/274653a0.

Currie, B. (2002), Structural con?guration of the Early Cretaceous Cordilleran foreland-basin system and Sevier thrust belt, Utah and Colorado, *J. Geol.*, *110*, 697–718, doi:10.1086/342626.

DeCelles, P. G., M. B. Gray, K. D. Ridgway, R. B. Cole, P. Srivastava, N. Pequera, and D. A. Pivnik (1991), Kinematic history of a foreland uplift from Paleocene synorogenic conglomerate, Beartooth Range, Wyoming and Montana, *Geol. Soc. Am. Bull.*, *103*, 1458–1475, doi:10.1130/0016-7606(1991)103<1458:KHOAFU>2.3.CO;2.

Dettman, D. L., and K. C. Lohmann (2000), Oxygen isotope evidence for high-altitude snow in the Laramide Rocky Mountains of North America during the Late Cretaceous and Paleogene, *Geology*, *28*, 243–246, doi:10.1130/0091-7613(2000)28<243:OIEFHS>2.0.CO;2.

English, J. M., and S. T. Johnston (2004), Laramide orogeny: What were the driving forces?, *Int. Geol. Rev.*, *46*, 833–838, doi:10.2747/0020-6814.46.9.833.

Flowers, R. M. (2009), Exploiting radiation damage control on apatite (U-Th)/He dates in cratonic regions, *Earth Planet. Sci. Lett.*, *277*, 148–155, doi:10.1016/j.epsl.2008.10.005.

Fricke, H. C. (2003), Investigation of early Eocene water-vapor transport and paleoelevation using oxygen isotope data from geographically widespread mammal remains, *Geol. Soc. Am. Bull.*, *115*, 1088–1096, doi:10.1130/B25249.1.

Goes, S., and S. van der Lee (2002), Thermal structure of the North American uppermost mantle inferred from seismic tomography, *J. Geophys. Res.*, *107*(B3), 2050, doi:10.1029/2000JB000049.

Grand, S. P. (2002), Mantle shear-wave tomography and the fate of subducted slabs, *Philos. Trans. R. Soc. London, Ser. A*, *360*, 2475–2491, doi:10.1098/rsta.2002.1077.

Grand, S. P., R. D. van der Hilst, and S. Widiyantoro (1997), Global seismic tomography: A snapshot of convection in the Earth, *GSA Today*, *7*(4), 1–7.

Gurnis, M. (1991), Continental flooding and mantle-lithosphere dynamics, in *Glacial Isostasy, Sea-Level, and Mantle Rheology*, edited by R. Sabadini, K. Lambeck, and E. Boschi, pp. 445–492, Kluwer Acad., Dordrecht, Netherlands.

Gurnis, M., R. D. Müller, and L. Moresi (1998), Dynamics of Cretaceous vertical motion of Australia and the Australian-Antarctic discordance, *Science*, *279*, 1499–1504, doi:10.1126/science.279.5356.1499.

Gurnis, M., J. X. Mitrovica, J. Ritsema, and H.-J. van Heijst (2000), Constraining mantle density structure using geological evidence of surface uplift rates: The case of the African Superplume, *Geochem. Geophys. Geosyst.*, *1*(7), 1020, doi:10.1029/1999GC000035.

Hager, B. H. (1984), Subducted slabs and the geoid: Constraints on mantle rheology and flow, *J. Geophys. Res.*, *89*(B7), 6003–6015, doi:10.1029/JB089iB07p06003.

Haq, B. U., and A. M. Al-Qahtani (2005), Phanerozoic cycles of sea-level change on the Arabian Platform, *Geoarabia*, *10*(2), 127–160.

Haq, B. U., J. Hardenbol, and P. R. Vail (1987), Chronology of fluctuating sea levels since the Triassic, *Science*, *235*, 1156–1167, doi:10.1126/science.235.4793.1156.

Harrison, C. G. A. (1990), Long-term eustasy and epeirogeny in continents, in *Sea-Level Change*, edited by R. Revelle, pp. 141–160, Natl. Acad. Press, Washington, D. C.

Heller, P. L., K. Dueker, and M. E. McMillan (2003), Post-Paleozoic alluvial gravel transport as evidence of continental tilting in the Cordillera, *U. S., Geol. Soc. Am. Bull.*, *115*, 1122–1132, doi:10.1130/B25219.1.

Humphreys, E. D., and D. D. Coblentz (2007), North American dynamics and western U.S. tectonics, *Rev. Geophys.*, *45*, RG3001, doi:10.1029/2005RG000181.

Ishii, M., and J. Tromp (2004), Constraining large-scale mantle heterogeneity using mantle and inner-core sensitive normal modes, *Phys. Earth Planet. Inter.*, *146*, 113–124, doi:10.1016/j.pepi.2003.06.012.

Ismail-Zadeh, A., G. Schubert, I. Tsepelev, and A. Korotkii (2004), Inverse problem of thermal convection: Numerical approach and application to mantle plume restoration, *Phys. Earth Planet. Inter.*, *145*, 99–114, doi:10.1016/j.pepi.2004.03.006.

Jordan, T. H. (1975), The continental tectosphere, *Rev. Geophys.*, *13*, 1–12, doi:10.1029/RG013i003p00001.

King, S. D., and G. Masters (1992), An inversion for radial viscosity structure using seismic tomography, *Geophys. Res. Lett.*, *19*(15), 1551–1554, doi:10.1029/92GL01700.

Kominz, M. A. (1984), Oceanic ridge volumes and sea level change: An error analysis, in *Interregional Unconformities and Hydrocarbon Accumulation*, edited by J. Schlee, *AAPG Mem.*, *36*, pp. 109–127.

Le Stunff, Y., and Y. Ricard (1997), Partial advection of equidensity surfaces: A solution for the dynamic topography problem?, *J. Geophys. Res.*, *102*(B11), 24,655–24,667, doi:10.1029/97JB02346.

Lithgow-Bertelloni, C., and M. Gurnis (1997), Cenozoic subsidence and uplift of continents from time-varying dynamic topography, *Geology*, *25*, 735–738, doi:10.1130/0091-7613(1997)025<0735:CSAUOC>2.3.CO;2.

Liu, L., and M. Gurnis (2008), Simultaneous inversion of mantle properties and initial conditions using an adjoint of mantle convection, *J. Geophys. Res.*, *113*, B08405, doi:10.1029/2008JB005594.

Liu, L., S. Spasojević, and M. Gurnis (2008), Reconstructing Farallon plate subduction beneath North America back to the Late Cretaceous, *Science*, *322*, 934–938, doi:10.1126/science.1162921.

Liu, S., and D. Nummedal (2004), Late Cretaceous subsidence in Wyoming: Quantifying the dynamic component, *Geology*, *32*, 397–400, doi:10.1130/G20318.1.

Liu, S., D. Nummedal, P.-G. Yin, and H.-J. Luo (2005), Linkage of Sevier thrusting episodes and Late Cretaceous foreland basin megasequences across southern Wyoming (USA), *Basin Res.*, *17*, 487–506, doi:10.1111/j.1365-2117.2005.00277.x.

Manea, V., and M. Gurnis (2007), Subduction zone evolution and low viscosity wedges and channels, *Earth Planet. Sci. Lett.*, *264*, 22–45, doi:10.1016/j.epsl.2007.08.030.

McMillan, M. E., P. L. Heller, and S. L. Wing (2006), History and causes of post-Laramide relief in the Rocky Mountain orogenic plateau, *Geol. Soc. Am. Bull.*, *118*, 393–405, doi:10.1130/B25712.1.

McQuarrie, N., and C. G. Chase (2000), Raising the Colorado Plateau, *Geology*, *28*, 91–94, doi:10.1130/0091-7613(2000)028<0091:RTCP>2.0.CO;2.

Mégnin, C., and B. Romanowicz (2000), The shear velocity structure of the mantle from the inversion of body, surface and higher modes waveforms, *Geophys. J. Int.*, *143*, 709–728, doi:10.1046/j.1365-246X.2000.00298.x.

Miller, K. G., M. A. Kominz, J. V. Browning, J. D. Wright, G. S. Mountain, M. E. Katz, P. J. Sugarman, B. S. Cramer, N. Christie-Blick, and S. F. Pekar (2005), The Phanerozoic record of global sea-level change, *Science*, *310*, 1293–1298, doi:10.1126/science.1116412.

Milne, G. A., J. X. Mitrovica, H.-G. Scherneck, J. L. Davis, J. M. Johansson, H. Koivula, and M. Vermeer (2004), Continuous GPS measurements of postglacial adjustment in Fennoscandia: 2. Modeling results, *J. Geophys. Res.*, *109*, B02412, doi:10.1029/2003JB002619.

Mitrovica, J. X., and A. M. Forte (2004), A new inference of mantle viscosity based upon joint inversion of convection and glacial isostatic adjustment data, *Earth Planet. Sci. Lett.*, *225*, 177–189, doi:10.1016/j.epsl.2004.06.005.

Mitrovica, J. X., C. Beaumont, and G. T. Jarvis (1989), Tilting of continental interiors by the dynamical effects of subduction, *Tectonics*, *8*, 1079–1094, doi:10.1029/TC008i005p01079.

Morgan, W. J. (1971), Convection plumes in the lower mantle, *Nature*, *230*, 42–43, doi:10.1038/230042a0.

Moucha, R., A. M. Forte, J. X. Mitrovica, D. B. Rowley, S. Quéré, N. A. Simmons, and S. P. Grand (2008), Dynamic topography and long-term sea-level variations: There is no such thing as a stable continental platform, *Earth Planet. Sci. Lett.*, *271*, 101–108, doi:10.1016/j.epsl.2008.03.056.

Müller, R. D., M. Sdrolias, C. Gaina, and W. R. Roest (2008a), Age, spreading rates and spreading asymmetry of the world's ocean crust, *Geochem. Geophys. Geosyst.*, *9*, Q04006, doi:10.1029/2007GC001743.

Müller, R. D., M. Sdrolias, C. Gaina, B. Steinberger, and C. Heine (2008b), Long-term sea-level fluctuations driven by ocean basin dynamics, *Science*, *319*, 1357–1362, doi:10.1126/science.1151540.

Ni, S., E. Tan, M. Gurnis, and D. Helmberger (2002), Sharp sides to the African superplume, *Science*, *296*, 1850, doi:10.1126/science.1070698.

O'Neill, C., R. D. Muller, and B. Steinberger (2005), On the uncertainties in hotspot reconstructions and the significance of moving hot spot reference frames, *Geochem. Geophys. Geosyst.*, *6*, Q04003, doi:10.1029/2004GC000784.

Pang, M., and D. Nummedal (1995), Flexural subsidence and basement tectonics Cretaceous Western Interior basin, *United States, Geology*, *23*(2), 173–176, doi:10.1130/0091-7613(1995)023<0173:FSABTO>2.3.CO;2.

Pindell, J., L. Kennan, K. P. Stanek, W. V. Maresch, and G. Draper (2006), Foundations of Gulf of Mexico and Caribbean evolution: Eight controversies resolved, *Geol. Acta*, *41*, 303–341.

Quéré, S., and A. M. Forte (2006), Influence of past and present-day plate motions on spherical models of mantle convection: Implications for mantle plumes and hotspots, *Geophys. J. Int.*, *165*(3), 1041–1057, doi:10.1111/j.1365-246X.2006.02990.x.

Ren, Y., E. Stutzmann, R. D. Van der Hilst, and J. Besse (2007), Understanding seismic heterogeneities in the lower mantle beneath the Americas from seismic tomography and plate tectonic history, *J. Geophys. Res.*, *112*, B01302, doi:10.1029/2005JB004154.

Richards, M., and B. Hager (1984), Geoid anomalies in a dynamic earth, *J. Geophys. Res.*, *89*, 5987–6002, doi:10.1029/JB089iB07p05987.

Ritsema, J., H. J. van Heijst, and J. H. Woodhouse (2004), Global transition zone tomography, *J. Geophys. Res.*, *109*, B02302, doi:10.1029/2003JB002610.

Roth, J. B., M. J. Fouch, D. E. James, and R. W. Carlson (2008), Three-dimensional seismic velocity structure of the northwestern United States, *Geophys. Res. Lett.*, *35*, L15304, doi:10.1029/2008GL034669.

Saleeby, J. (2003), Segmentation of the Laramide slab-evidence from the southern Sierra Nevada region, *Geol. Soc. Am. Bull.*, *115*, 655–668, doi:10.1130/0016-7606(2003)115<0655:SOTLSF>2.0.CO;2.

Sigloch, K., N. McQuarrie, and G. Nolet (2008), Two-stage subduction history under North America inferred from multiple-frequency tomography, *Nat. Geosci.*, *1*, 458–462, doi:10.1038/ngeo231.

Sirkes, Z., and E. Tziperman (1997), Finite difference of adjoint or adjoint of finite difference?, *Mon. Weather Rev.*, *125*, 3373–3378.

Sloss, L. L. (1988), Tectonic evolution of the craton in Phanerozoic time, in *Sedimentary Cover—North America Craton*, vol. D-2, *The Geology of North America*, edited by L. L. Sloss, pp. 25–51, Geol. Soc. of Am., Boulder, Colo.

Smith, A. G., D. G. Smith, and B. M. Funnel (1994), *Atlas of Mesozoic and Cenozoic coastlines*, 99 pp., Cambridge Univ. Press, New York.

Solomon, S. C., and N. H. Sleep (1974), Some simple physical models for absolute plate motions, *J. Geophys. Res.*, *79*, 2557–2567, doi:10.1029/JB079i017p02557.

Spasojević, S., L. Liu, M. Gurnis, and R. D. Müller (2008), The case for dynamic subsidence of the United States east coast since the Eocene, *Geophys. Res. Lett.*, *35*, L08305, doi:10.1029/2008GL033511.

Sun, J., D. W. Flicker, and D. K. Lilly (1991), Recovery of 3D wind and temperature fields from simulate single-Doppler radar data, *J. Atmos. Sci.*, *48*, 876–890, doi:10.1175/1520-0469(1991)048<0876:ROTDWA>2.0.CO;2.

Talagrand, O., and P. Courtier (1987), Variational assimilation of meteorological observation with the adjoint vorticity equation, *Q. J. R. Meteorol. Soc.*, *113*, 1311–1328, doi:10.1256/smsqj.47811.

Trampert, J., F. Deschamps, J. Resovsky, and D. Yuen (2004), Probabilistic tomography maps chemical heterogeneities throughout the lower mantle, *Science*, *306*, 853–856, doi:10.1126/science.1101996.

Van der Hilst, R. D., S. Widiyantoro, and E. R. Engdahl (1997), Evidence of deep mantle circulation from global tomography, *Nature*, *386*, 578–584, doi:10.1038/386578a0.

Van Sickel, W. A., M. Kominz, K. G. Miller, and J. V. Browning (2004), Late Cretaceous and Cenozoic sea-level estimates: Backstripping analysis of borehole data, onshore New Jersey, *Basin Res.*, *16*, 451–465, doi:10.1111/j.1365-2117.2004.00242.x.

Watts, A. B., and M. S. Steckler (1979), Subsidence and eustasy at the continental margin of eastern North America, in *Deep Drilling Results in the Atlantic Ocean: Continental Margins and Paleoenvironment*, *Maurice Ewing Ser.*, vol. 3, edited by M. Talwani, W. Hay, and W. B. F. Ryan, pp. 218–234, AGU, Washington, D. C.

Zhong, S., M. T. Zuber, L. Moresi, and M. Gurnis (2000), Role of temperature-dependent viscosity and surface plates in spherical shell models of mantle convection, *J. Geophys. Res.*, *105*, 11,063–11,082, doi:10.1029/2000JB900003.